HHS Public Access

Author manuscript

Mol Cell. Author manuscript; available in PMC 2023 April 07.

Published in final edited form as:

Mol Cell. 2022 April 07; 82(7): 1261–1277.e9. doi:10.1016/j.molcel.2022.02.028.

Hexokinase 1 cellular localization regulates the metabolic fate of glucose

Adam De Jesus[1,2,7], **Farnaz Keyhani-Nejad**[1,2,7], **Carolina M. Pusec**[1], **Lauren Goodman**[1,2], **Justin A. Geier**[1,2], **Joshua S. Stoolman**[1], **Paulina J. Stanczyk**[1,2], **Tivoli A. T. Nguyen**[1,2], **Kai Xu**[3], **Krishna V. Suresh**[1,2], **Yihan Chen**[1], **Arianne E. Rodriguez**[1], **Jason S. Shapiro**[1,2], **Hsiang-Chun Chang**[1,2], **Chunlei Chen**[1], **Kriti P. Shah**[1], **Issam Ben-Sahra**[3], **Brian T. Layden**[1,5,6], **Navdeep S. Chandel**[1], **Samuel E. Weinberg**[4], **Hossein Ardehali**[1,2,8,9]

[1]Department of Medicine, Northwestern University Feinberg School of Medicine, Chicago, IL 60611, USA.

[2]Feinberg Cardiovascular Research Institute, Northwestern University, Chicago, IL, 60611, USA.

[3]Department of Biochemistry and Molecular Genetics, Northwestern University Feinberg School of Medicine, Chicago, IL, 60611, USA.

[4]Department of Pathology, Northwestern University Feinberg School of Medicine, Chicago, IL, 60611, USA.

[5]Department of Medicine, University of Illinois at Chicago, Chicago, IL 60612, USA.

[6]Jesse Brown Veterans Affairs Medical Center, Chicago, IL, 60612, USA.

[7]These authors contributed equally.

[9]Lead Contact.

SUMMARY

The product of hexokinase (HK) enzymes, glucose-6-phosphate, can be metabolized through glycolysis or directed to alternative metabolic routes, such as the pentose phosphate pathway (PPP) to generate anabolic intermediates. HK1 contains an N-terminal mitochondrial–binding domain (MBD), but its physiologic significance remains unclear. To elucidate the effect of

[8] Corresponding author h-ardehali@northwestern.edu.

AUTHOR CONTRIBUTIONS

Conceptualization: A.D., S.E.W., C.M.P., A.E.R., Jason.S.S., H.C.C., B.T.L., and H.A.
Methodology: A.D., C.M.P., A.E.R., I.B.S., Jason.S.S., and H.C.C.
Investigation: A.D., C.M.P., F.K.N., L.G., J.A.G., Josh.S.S., K.X., K.V.S., Y.C., C.C., K.P.S., and P.J.S., T.A.T.N.
Results Interpretation: H.A., A.D., C.M.P., Jason.S.S., and F.K.N.
Resources: B.T.L., I.B.S., N.S.C., S.E.W., and H.A.
Writing—Original Draft, H.A., A.D., and C.M.P.
Writing—Review and Editing: C.M.P., Jason.S.S., F.K.N., and H.A.
Visualization: A.D.
Supervision: S.E.W., B.T.L., and H.A.

DECLARATION OF INTERESTS

The authors declare no competing interests.

HK1 mitochondrial dissociation on cellular metabolism, we generated mice lacking the HK1 MBD (ΔE1HK1). These mice produced a hyper-inflammatory response when challenged with lipopolysaccharide. Additionally, there was decreased glucose flux below the level of GAPDH and increased upstream flux through the PPP. The glycolytic block below GAPDH is mediated by binding of cytosolic HK1 with S100A8/A9 resulting in GAPDH nitrosylation through iNOS. Additionally, human and mouse macrophages from conditions of low-grade inflammation, such as aging and diabetes, displayed increased cytosolic HK1 and reduced GAPDH activity. Our data indicate that HK1 mitochondrial binding alters glucose metabolism through regulation of GAPDH.

eTOC:

De Jesus et al. describe how HK1 subcellular localization regulates the metabolic fate of its substrate, G6P, between catabolic and anabolic metabolism through inhibition of GAPDH. Immune cells from models of aging and diabetes show higher levels of cytosolic HK1 and increased inflammation

Graphical Abstract

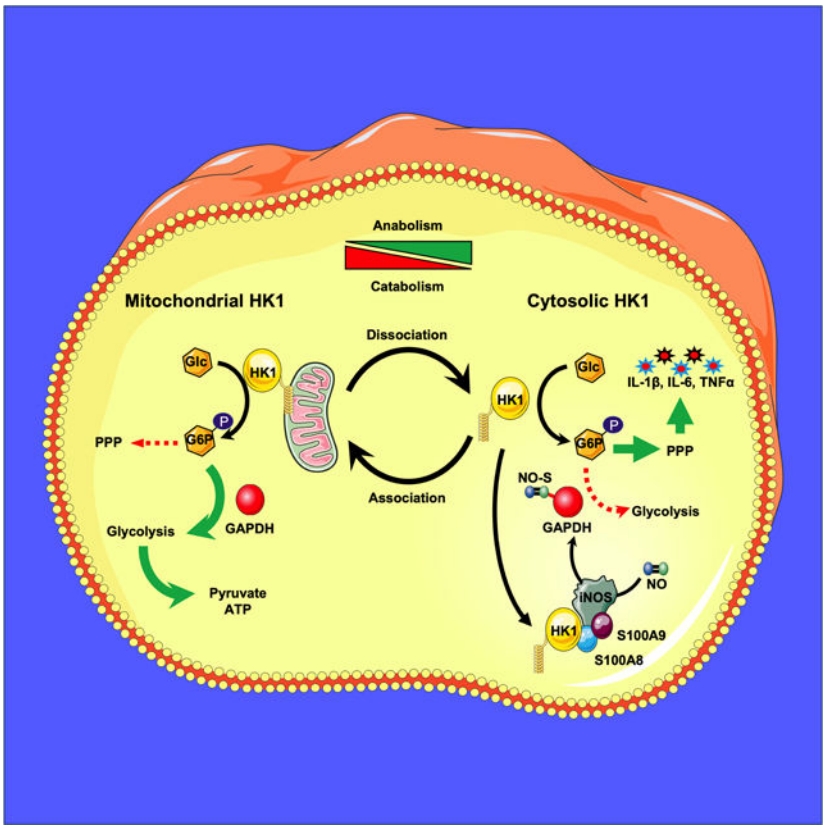

Keywords

Mitochondria; metabolism; hexokinase; GAPDH; inflammation; S-nitrosylation; pentose phosphate pathway; macrophage; innate immunity; subcellular localization

INTRODUCTION

Hexokinases (HKs) represent the first committed step in glucose utilization by catalyzing the phosphorylation of glucose to glucose-6-phosphate (G6P). This phosphorylation sequesters glucose in the cell and commits it to various downstream metabolic pathways (Bell et al., 1993; Gould and Holman, 1993; Mueckler, 1994; Printz et al., 1997). G6P can enter glycolysis for energy production, the pentose phosphate pathway (PPP) for anabolic intermediates or be converted to glucose-1-phosphate for glycogen synthesis (Adeva-Andany et al., 2016; Puleston et al., 2017). In mammals, five HK isozymes (HK1, HK2, HK3, glucokinase (GCK), and hexokinase domain-containing 1 (HKDC1)) have been identified, each with distinct patterns of tissue expression, subcellular localization, enzyme kinetics, and substrate specificities (Middleton, 1990; Ureta, 1982; Wilson, 2003). HK1, HK2 and HKDC1 contain an N-terminal, 21-amino-acid hydrophobic sequence that enables outer mitochondrial membrane (OMM) binding (Pusec et al., 2019; Rose and Warms, 1967a; Sui and Wilson, 1997), possibly through its interaction with the family of mitochondrial bound voltage dependent anion channel (VDAC) proteins (Aflalo and Azoulay, 1998; Azoulay-Zohar et al., 2004; Fiek et al., 1982; Lindén et al., 1982). This sequence, termed the mitochondrial binding domain (MBD), is encoded in exon 1, while exons 2 through half of exon 10 encode for the N-terminal domain and the remaining part of exon 10 through exon 18 encode for the C-terminal domain (Printz et al., 1993, 1995).

Prior studies have proposed that this HK1/HK2 mitochondrial binding functions to allow for preferential access to mitochondrial pools of ATP (Rose and Warms, 1967b), however, the cytosolic concentration of ATP is generally higher than the K_{mATP} for these enzymes, suggesting that HKs do not need to shift their localization to utilize ATP efficiently (Lobas et al., 2019; Manfredi et al., 2002). HK mitochondrial binding is also proposed to increase TCA cycle activity, as compared to cytosolic pools of HK, leading to increased protein translation (Golshani-Hebroni and Bessman, 1997). Additionally, binding of HKs to VDAC on the OMM has been shown to prevent opening of the permeability transition pore (PTP) and prevent release of cytochrome-C after treatment with apoptotic stimuli (Sun et al., 2008). However, most of these studies have been conducted with HK2, and there are limited studies on HK1 (Halestrap et al., 2015; Pasdois et al., 2013; Tanaka et al., 2018). HK2 binding to VDAC also blocks recruitment of apoptotic mediators, Bax and Bak from binding to VDAC, which further blunts the cell death response (Pastorino et al., 2002). However, most of these studies were done with protein overexpression or using a nonspecific peptide to dislocate HKs from the mitochondria. Additionally, it is counterintuitive that HK mitochondrial binding would permit flow of ATP/ADP through VDAC pore (to allow ATP access to HKs), while preventing cytochrome-C release through VDAC pore closure. Since the purpose of mitochondrial-bound HK1 is still unclear, we reoriented our focus and hypothesized that cytosolic localization of HK1 could result in novel gain-of-function like actions that were independent of mitochondrial-related functions of HK1. To test this hypothesis, we generated a mouse model that lacks the MBD of HK1.

Metabolic adaptations are inextricably linked to the immediate host defense against foreign pathogens (Pearce and Pearce, 2013; Sancho et al., 2017; Stienstra et al., 2017). In the setting of innate inflammatory activation, there is a robust increase in glycolysis even in

the setting of abundant oxygen, a metabolic program shared by rapidly proliferating cells termed aerobic glycolysis (Andrejeva and Rathmell, 2017; Cheng et al., 2014; Everts et al., 2014; Garaude et al., 2016; O'Neill and Pearce, 2016; Pavlova and Thompson, 2016). In addition to elevated glycolytic rate, there is increased glucose flux through the PPP and other ancillary metabolic pathways in immune cells following toll-like receptor (TLR) stimulation (Hughes and O'Neill, 2018; Puleston et al., 2017). Recently, HK2 was shown to play an important role in inflammasome activation (Wolf et al., 2016), and in viral-mediated inflammation (Zhang et al., 2019). In macrophages, HK1 mRNA is highly expressed after pro-inflammatory stimulation (Nishizawa et al., 2014), and HK1-dependent glycolysis is important for proper inflammasome activation in macrophages (Moon et al., 2015). HK1 has also been shown to facilitate metabolite flux into the mitochondria in CD8+ T-cells (Bantug et al., 2018). These results indicate a major role for HK-mediated glucose metabolism in the activation of inflammatory cells.

Despite extensive research on glucose metabolism, it remains unclear what factor(s) decide the fate of glucose and regulate the entrance of G6P into a specific pathway. Elucidating this regulation will be important for developing therapeutic approaches to many disorders associated with inflammation, such as diabetes and heart disease. In this paper, we demonstrate that the binding of HK1 to the mitochondria determines whether the product of the enzyme (G6P) is catabolized through glycolysis or shunted through PPP. We show that dislocation of HK1 to the cytoplasm shifts G6P toward the PPP through cytosolic HK1 interaction with S100A8/9, which mediates iNOS dependent nitrosylation of GAPDH and its subsequent inactivation. Therefore, HK1 functions as an important metabolic switch between catabolic and anabolic metabolism through its subcellular localization.

RESULTS

Mice with HK1 MBD-deletion display no overt phenotype at baseline

To determine the cellular consequences of HK1 mitochondrial binding, we generated GFP-tagged constructs of full-length HK1 (FLHK1) and truncated HK1 (TrHK1) that lack the MBD (Figure S1A). These constructs were transfected into HepG2 cells, and their cellular distribution was assessed by GFP fluorescence. As expected, FLHK1 localized to the mitochondria, while TrHK1 displayed diffuse cellular distribution (Figure S1B and S1C). TrHK1 displayed similar HK activity as FLHK1 (Figure S1D and S1E), supporting that deletion of the MBD does not affect the ability of HK1 to phosphorylate glucose. These results indicate that altering the subcellular localization of HK1 by removing the MBD does not impair its enzymatic activity.

To determine the physiologic function of the HK1 MBD, we generated a mouse model lacking the MBD of the endogenous HK1 (Figure 1A). Homozygote mice with this mutation, designated as ΔE1HK1 herein, were born in normal Mendelian ratios and displayed no overt changes in weight or difference in whole body glucose homeostasis as assessed by glucose tolerance test (GTT) and insulin tolerance test (ITT) (Figure 1B–1D). Moreover, hematologic analysis of whole blood from these mice revealed no difference in complete blood cell count (CBC) or white blood cell (WBC) differential (Figure S1F and S1G). To assess whether removal of the endogenous HK1 MBD alters cellular distribution

of the protein, we isolated mitochondrial and cytosolic fractions from spleen tissue and show that HK1 is predominantly present in the cytosolic fraction isolated from ΔE1HK1 mice (Figure 1E). We also performed HK activity assay in spleen tissue lysates and found no difference in activity between the ΔE1HK1 and WT mice (Figure 1F).

Immunofluorescence (IF) studies in bone marrow-derived macrophages (BMDMs) and peritoneal macrophages (PMs) isolated from WT and ΔE1HK1 mice also confirmed lack of HK1 localization to the mitochondria (Figure 1H–1I and S1H–S1I). Additionally, BMDMs isolated from WT and ΔE1HK1 mice displayed similar glucose uptake and phosphorylating activity, consistent with our findings in spleen tissue from ΔE1HK1 mice and HepG2 overexpression cells (Figure 1J and 1K). We also assessed *in vivo* glucose transport by injecting WT and ΔE1HK1 mice with 2-NBDG, followed by isolation of PMs and measurement of intracellular fluorescence. 2-NBDG has been shown to be taken up and phosphorylated (Zou et al., 2005), so the measurement of cellular fluorescence reflects both uptake and phosphorylation of the molecule by HKs. Consistent with our *in vitro* data, we did not see a change in glucose transport in isolated BMDMs (Figure S1J). Additionally, we demonstrated that HK1 dislocation from the mitochondria does not cause an increase in reactive oxygen species (ROS) production or affect cell viability in BMDMs (Figure S1K and S1L). Finally, we show that HK1 mitochondrial dislocation does not affect its protein stability by measuring HK1 protein levels in BMDMs from WT and ΔE1HK1 mice after treatment with cycloheximide (CHX) (Figure S1M).

We next assessed whether HK1 mitochondrial dislocation and inflammation has effects on other HK isoforms. Among the five different HK isoforms, only HK1 and HK3 displayed a dose-dependent increase in their mRNA levels in response to lipopolysaccharide (LPS) in WT BMDMs (Figure S1N). Additionally, while HK1 showed a reversible dislocation from the mitochondria in response to LPS (Figure S2A and S2B), HK2 (another HK isoform that binds to the mitochondria) showed no dissociation from the mitochondria in response to LPS in WT or ΔE1HK1 BMDMs (Figure S2C and S2D). Moreover, whole cell lysates and subcellular fractionation of WT and ΔE1HK1 BMDMs showed no difference in HK2 localization or total protein amount (Figure S2E and S2F). Lastly, HepG2 cells did not show a change in total HK2 protein levels between FLHK1 and TrHK1 overexpressing cells (Figure S2G and S2H). Overall, these results suggest an important role for HK1 in LPS-activated macrophages and provide an ideal system to study the MBD of HK1 in the absence of confounding changes to other mitochondrial bound HKs.

HK1 mitochondrial dissociation shifts glucose flux to PPP

Since there was no difference in glucose phosphorylation with HK1 MBD deletion, we then assessed whether downstream glucose metabolism was altered by the removal of the HK1 MBD. HepG2 cells expressing TrHK1 displayed reduced glycolysis, measured by extracellular lactate production and extracellular acidification rate (ECAR) (Figure S3A and S3B). Similarly, ΔE1HK1 BMDMs had significantly lower lactate production (Figure 2A) and a significant reduction in ECAR upon immediate stimulation with LPS (Figure 2B), which persisted up to at least 5 hours after LPS treatment (Figure 2C). However, there was no difference in the oxygen consumption rate (OCR) between the WT and

ΔE1HK1 BMDMs in the presence or absence of LPS (Figure 2D). To further elucidate the mechanism responsible for the reduction in glycolysis observed in LPS-activated ΔE1HK1 BMDMs, we performed $^{13}C_6$-glucose tracing metabolomics in naïve and LPS-stimulated BMDMs derived from WT and ΔE1HK1 mice. We measured ^{13}C-glucose incorporation through glycolysis, tricarboxylic acid (TCA) cycle, and PPP (Figure 2E). While there was no difference in G6P levels between WT and ΔE1HK1 BMDMs (Figure 2F), ΔE1HK1 BMDMs displayed higher $^{13}C_6$-glucose incorporation into glyceraldehyde-3-phosphate/dihydroxyacetone phosphate (GAP/DHAP) (Figure 2G) and PPP intermediates 6-phosphogluconate (6-PG) and sedoheptulose-7-Phosphate after LPS activation (Figure 2H and 2I). NADPH/NADP+ ratio was also significantly increased in ΔE1HK1 BMDMs (Figure 2J). Moreover, we observed decreased $^{13}C_6$-glucose incorporation of glycolytic intermediates below the level of GAPDH including 2/3-phosphoglycerate (2/3-PG), pyruvate, and lactate in LPS-treated BMDMs from ΔE1HK1 as compared to WT controls (Figure 2K–2M). Although TCA cycle intermediate citrate showed decreased $^{13}C_6$-glucose incorporation (Figure 2N), we did not observe a change in glucose-derived carbon incorporation into α-ketoglutarate (αKG), succinate, or fumarate between WT and ΔE1HK1 BMDMs (Figure 2O–2Q). Since unlabeled glutamine can supply carbons into the TCA cycle through anaplerotic conversion to αKG (Jha et al., 2015), this may explain the lack of change in $^{13}C_6$-glucose labeling of TCA cycle metabolites downstream of citrate. These results are consistent with our earlier extracellular flux studies in HepG2 cells and BMDMs showing reduced glycolytic rate and extracellular lactate production with HK1 mitochondrial dissociation. We also performed tracing experiments using 1,2-^{13}C-glucose in BMDMs from WT and ΔE1HK1 mice (Figure S3C) and demonstrated higher one-carbon labeled Ribose-5P, ATP, Lactate, and Pyruvate in ΔE1HK1 mouse PMs, which indicate higher oxidative PPP flux (Figure S3D–S3K).

We also performed $^{13}C_6$-glucose labeling metabolomics in HepG2 cells with FLHK1 or TrHK1 overexpression and assessed similar metabolic pathways (Figure S4A). In alignment with our results in BMDMs, there was a significant increase in glycolytic intermediates above the level of GAPDH (GAP and glycerate) (Figure S4B), and an increase of $^{13}C_6$-glucose incorporation into the PPP intermediate sedoheptulose-7-P and several nucleotides in cells overexpressing TrHK1 (Figure S4C), consistent with increased *de novo* nucleotide synthesis through the PPP. Consistent with data obtained from BMDMs, we also found less $^{13}C_6$-glucose incorporation into lower glycolytic products such as 2/3-PG, pyruvate, and lactate (Figure S4D) and TCA cycle intermediates (Figure S4E). Additionally, we saw increased NADPH/NADP+ ratio (Figure S4F), similar to BMDMs. Overall, these results indicate that dissociation of HK1 from mitochondria alters glycolysis and increases G6P incorporation into PPP at the expense of lower glycolysis.

HK1 mitochondrial dissociation increases cytokine production

Our results thus far indicate that HK1 dislocation into the cytoplasm shifts glucose utilization in favor of increased PPP metabolites. We next wanted to understand how this metabolic change alters cell function. To further study this process, we focused on macrophages since PPP metabolism has been shown to be upregulated in LPS activated macrophages and is necessary for proper inflammatory activation (Baardman et al., 2018;

Ham et al., 2013; Martinez et al., 2006; Nagy and Haschemi, 2015). We noted a significant increase in inflammatory cytokines IL-1β, IL-6 and TNFα mRNA expression in BMDMs from ΔE1HK1 mice in response to LPS compared to WT (Figure 3A–3C). In addition, BMDMs from ΔE1HK1 mice displayed increased IL-1β protein production after LPS treatment (Figure 3D). As expected, LPS-activated BMDMs from ΔE1HK1 and WT mice showed a similar increase in mRNA expression of HK1, while there was no change in the levels of HK2 mRNA (Figure S5A and S5B). We also assessed mRNA levels of the anti-inflammatory markers peroxisome proliferator-activated receptor gamma (PPARγ) and carbohydrate kinase-like protein (CARKL) in BMDMs and found no difference in their expression between ΔE1HK1 and WT cells (Figure S5C and S5D). Intracellular protein expression of pro-IL-1β in control and LPS-treated BMDMs showed an increase in ΔE1HK1 compared to WT cells, and addition of ATP-induced cleavage and secretion of IL-1β in both groups (Figure S5E and S5F). Moreover, using extracellular media from BMDMs treated with LPS+ATP, we demonstrate that IL-1β protein secretion increased in ΔE1HK1 BMDMs compared to WT controls (Figure S5G).

PMs isolated from ΔE1HK1 mice also showed similar increases in inflammatory cytokine expression relative to WT (Figure 3E–3G). PMs from ΔE1HK1 mice also had increased IL-1β protein secretion after LPS treatment, as assessed by ELISA (Figure 3H). Furthermore, we extracted mRNA from the spleens of mice treated with 4hrs of LPS, and found a significant increase in the same inflammatory markers in ΔE1HK1 mice (Figure 3I–3K). Lastly, we performed an *in vivo* LPS-induced endotoxemia survival experiment in these mice (Figure 3L). Three-days after sub-lethal LPS administration, ΔE1HK1 mice had significantly reduced survival compared to littermate controls (Figure 3M). Collectively, these results indicate that lack of HK1 mitochondrial binding increases inflammatory cytokine production and impairs survival in response to LPS-induced endotoxemia.

PPP inhibition reverses increased inflammation in ΔE1HK1 mice

The PPP is upregulated in pro-inflammatory macrophages, and reduction of PPP metabolites reduces activated macrophage cytokine production (Nagy and Haschemi, 2015; Baardman et al., 2018). Thus, to determine whether the hyper-inflammatory response seen in ΔE1HK1 mice is dependent on the increased PPP metabolism, we used two pharmacologic methods to inhibit the PPP, 6-aminonicotinamide (6AN) and oxythiamine (OT) (Figure 4A) (Tyson et al., 2000; Wang et al., 2013). Inhibition of PPP with 6AN or OT resulted in a reversal of the hyper-inflammatory response seen in BMDMs from ΔE1HK1 mice as measured by IL-1β protein (Figure 4B and 4C). The increase in IL-1β and IL-6 mRNA levels in BMDMs of ΔE1HK1 mice was also reversed when treated with either 6-AN (Figure 4D and 4E) or OT (Figure 4F and 4G). Additionally, IFNɣ-primed BMDMs showed a similar response when treated with 6AN or OT (Figure 4H and 4I). Moreover, the increase in NADPH/NADP+ ratio in BMDMs of ΔE1HK1 mice with and without LPS treatment were reversed with 6AN or OT (Figure 4J). We also show that there is no significant difference in the mRNA expression of key enzymes involved in glycolysis, PPP, pyruvate transport, and TCA cycle metabolism between WT and ΔE1HK1 BMDMs (Figure S6A–S6F), indicating that the mechanism for the glycolytic block causing increased PPP metabolism is likely not at the transcriptional level. Finally, we demonstrate that treatment with 6-phosphogluconate

dehydrogenase (6-PGD) siRNA also reverses the increase in IL-1β, IL-6 and TNFα mRNA levels in BMDMs from ΔE1HK1 relative to WT (Figure S7). Together, these studies suggest that the mechanism by which HK1 dislocation from mitochondria increases cytokine production is dependent on increased PPP metabolism.

GAPDH activity is attenuated in cells with HK1 mitochondrial dissociation

We next studied the mechanism by which cytosolic HK1 reduces glycolysis and shifts G6P towards the PPP. Analysis of the $^{13}C_6$-glucose labeling metabolomics indicated an increase in metabolites in upper glycolysis (i.e., metabolites upstream of the GAPDH-mediated step in glycolysis) and a reduction in metabolites in lower glycolysis (i.e., downstream of GAPDH), suggesting a block in glycolysis at the level of GAPDH. We first assessed whether manipulation of GAPDH influences cytokine production *in vitro* by using two GAPDH inhibitors, CGP3466 and koningic acid (KA), in RAW264.7 cells. Both CGP3466 (Figure S8A–S8B) and KA (Figure S8C–S8E) resulted in decreased GAPDH activity, while displaying increased inflammatory cytokine mRNA production. As expected, PMs and BMDMs from ΔE1HK1 mice displayed significantly decreased GAPDH activity at baseline and after LPS stimulation (Figure 5A and 5B). The difference in GAPDH activity of BMDMs between WT and ΔE1HK1 mice was abolished by CGP3466 (Figure 5C). CGP3466 also increased IL-1β mRNA expression in WT BMDMs to the level of the hyper-inflamed ΔE1HK1 BMDMs (Figure 5D). Finally, treatment of WT mice with the GAPDH inhibitor KA resulted in decreased survival, consistent with an exaggerated endotoxemia response due to elevated baseline inflammation (Figure 5E).

We also performed steady-state metabolomics in HepG2 cells with TrHK1 overexpression and observed a similar metabolic block at the level of GAPDH (Figure S8F and S8G). While there was an increase in the reductive state of the cell (increased NADH/NAD+ levels) with overexpression of TrHK1 (Figure S8H), the energy charge was unchanged between FLHK1 and TrHK1 overexpression cells (Figure S8I). Consistent with findings in BMDMs, overexpression of TrHK1 was associated with a significant decrease of GAPDH activity (Figure S8J). Together, these data indicate that HK1 mitochondrial binding is an important regulator of GAPDH function, and that dislocation of HK1 from the mitochondria causes an inhibition of GAPDH activity.

We next assessed the effects of acute dislocation of HK1 from the mitochondria on GAPDH activity and inflammation using clotrimazole (CLT), a chemical known to dissociated HKs from the mitochondria. (Huang et al., 2002; Shoshan-Barmatz et al., 2010; Sen et al., 2015). As expected, CLT caused a significant increase in HK1 dislocation from the mitochondria in RAW264.7 cells (Figure 5F and 5G). Despite minimal change in cytokine mRNA levels with CLT at baseline, stimulation with LPS induced a significant increase in the mRNAs of IL-1β, IL-6 and TNFα in the CLT-treated cells as compared to controls (Figure 5H–5J). Finally, CLT also caused a significant decrease in GAPDH activity in RAW264.7 cells after LPS treatment (Figure 5K). These results indicate that both acute and constitutive displacement of HK1 from the mitochondria cause a significant reduction in GAPDH activity and accentuates inflammatory cytokine production after LPS treatment.

HK1 mitochondrial dissociation mediates GAPDH nitrosylation by S100A8/A9

To study the mechanism of GAPDH inactivation, we performed HK1 co-immunoprecipitation (co-IP) followed by proteomics in HepG2 cells with overexpression of FLHK1 and TrHK1 (Figure S9A). Biological gene-ontology (GO) term analysis revealed several differences between the two treatments, as depicted in Figure S9B (Mi et al., 2019). VDAC proteins (VDAC1, VDAC2, and VDAC3) were enriched in the FLHK1 pulldown, which is expected since HK1 in its native form binds to these proteins on the OMM (Figure S9C) (Shoshan-Barmatz et al., 2009; Zhang et al., 2016). Among proteins enriched in cells overexpressing TrHK1, there was an over-representation of the S100 family of proteins, specifically S100A8 and S100A9, which are known to have inflammatory functions (Figure S9C) (Wang et al., 2018). We confirmed that S100A8 binds strongly to the truncated HK1 via co-IP in HepG2 cells overexpressing either FLHK1 or TrHK1 (Figure S9D–S9F).

We then confirmed this finding in BMDMs from ΔE1HK1 mice and found S100A8 as a binding partner of cytosolic HK1 in these cells (Figure 6A and 6B). S100A8 and S100A9 form a protein dimer called calprotectin that can bind to iNOS in macrophages and mediate trans-S-nitrosylation of GAPDH (SNO-GAPDH) and inhibition of its glycolytic activity (Jia et al., 2014). In cells with TrHK1 overexpression, we found higher GAPDH nitrosylation as compared to FLHK1 and GFP control expressing cells (Figure S9G). Importantly, BMDMs from ΔE1HK1 mice also displayed higher GAPDH nitrosylation than WT controls, which was reversible with 1400W treatment, a selective iNOS inhibitor (Thomsen et al., 1997) (Figure 6C and 6D). To assess whether the hyper-inflammation seen in ΔE1HK1 BMDMs is dependent on protein nitrosylation through iNOS, we administered 1400W to mice 1 hour prior to intraperitoneal injection of a sub-lethal dose of LPS for 3 hours and collected blood and splenic tissue from these mice for analysis (Figure 6E). ΔE1HK1 mice treated with 1400W showed a reduction in the hyper-inflammatory cytokine response as measured by splenic mRNA (Figure 6F–6H) and serum ELISA of inflammatory cytokines (Figure S9H). Additionally, ΔE1HK1 BMDMs treated with 1400W showed reversal of the hyper-inflammatory response (Figure 6I–6K). GAPDH activity of LPS treated ΔE1HK1 BMDMs was also restored to WT levels after 1400W treatment (Figure 6L). Next, we assessed whether iNOS inhibition could reverse the altered glycolytic effects seen in ΔE1HK1 BMDMs. We found that iNOS inhibition reversed the differences in ECAR observed between ΔE1HK1 and WT BMDMs after LPS treatment (Figure 6M and 6N). Additionally, 1400W was able to reverse the decreased survival seen in ΔE1HK1 mice after *in vivo* LPS-induced endotoxemia (Figure 6O). To evaluate the dependence of the hyper-inflammatory response on S100A8, we used siRNA to knock-down (KD) of S100A8 (Figure S9I) and observed a reversal of the hyper-inflammation seen in ΔE1HK1 cells (Figure S9J). Finally, treatment of WT BMDMs with 1400W reversed the increase in inflammatory cytokines (Figure S10A) and the reduction in GAPDH (Figure S10B) activity induced by CLT. Together, these data indicate that cytosolic HK1 binds to the S100A8 and likely promotes iNOS mediated nitrosylation and inactivation of GAPDH.

To further support that GAPDH nitrosylation mediates the change in cytokine production with the cytosolic form of HK1, we made GAPDH point mutant constructs that replaced the cysteine on position 247 with alanine. This cysteine has previously been reported to

be part of the nitrosylation motif recognized by S100A8/A9-iNOS (Jia et al., 2014), and its mutation makes GAPDH resistant to nitrosylation, thereby preventing its enzymatic inhibition. Overexpression of the $GAPDH^{C247A}$ mutant construct in BMDMs resulted in an increase in GAPDH activity that did not decrease in ΔE1HK1 BMDMs (Figure S10C), supporting the idea that the inhibitory effects of cytosolic HK1 on GAPDH is through nitrosylation. We then measured the mRNA levels of various cytokines in WT and ΔE1HK1 BMDMs with overexpression of the $GAPDH^{C247A}$ mutant construct. Overexpression of the $GAPDH^{C247A}$ construct reversed the increased inflammatory cytokine production seen in ΔE1HK1 BMDMs (Figure S10D). These results provide further evidence that the cytosolic HK1 mediates increased cytokine production through GAPDH nitrosylation and inhibition.

Although increased iNOS levels are induced by LPS (Hwang et al., 2017; Wang et al., 1999), our studies have demonstrated that GAPDH activity is also lower in macrophages from ΔE1HK1 at baseline (Figure 5A–C). We first showed that iNOS protein is expressed in BMDMs from WT and ΔE1HK1 mice at baseline (Figure S11A). We then isolated PMS from mice injected with 1400W *in vivo* for 4hrs and showed that ΔE1HK1 PMs have lower GPADH activity, which was reversed in the 1400W treatment group (Figure S11B). Additionally, we performed siRNA KD of iNOS in WT and ΔE1HK1 BMDMs (Figure S11C–S11E) and showed that KD of iNOS reversed the increase in mRNA levels of the inflammatory markers and the reduction in GAPDH seen in controls (Figure S11F and S11G). To confirm the role of iNOS in cytosolic HK1-mediated GAPDH inhibition, we conducted studies in HepG2 cells at baseline conditions, without LPS induction of iNOS activity. We first showed that the iNOS protein is expressed in HepG2 cells at baseline and does not change with overexpression of FLHK1 or TrHK1 (Figure S11H). Additionally, although GAPDH activity was reduced at baseline in HepG2 cells with TrHK1 overexpression, treatment with 1400W resulted in increased GAPDH activity (Figure S11I). These results are consistent with our earlier metabolic data demonstrating a reduction in lower glycolysis in unstimulated ΔE1HK1 BMDMs (Figure 2J–2L). Thus, an increase in baseline iNOS activity by cytosolic dislocation of HK1 is sufficient to inhibit GAPDH, even in the absence of LPS.

It may be argued that the effects of HK1 mitochondrial dislocation on cytokine production may not be through its cytosolic effects on GAPDH, but rather due to changes in mitochondrial function. To assess this possibility, we made an HK1 construct that is constitutively targeted to the mitochondria by cloning the transmembrane domain of the outer-mitochondrial Membrane Protein 25 (OMP25) in-frame with the C-terminal end of TrHK1 construct fused to GFP (Figure S12A). This construct was overexpressed in BMDMs from WT and ΔE1HK1 mice ± LPS. If HK1 mitochondrial localization is important for its physiological role, then this construct would be expected to rescue the phenotype. The OMPHK1 construct localized to the mitochondria (Figure S12B and S12C) but did not reverse the hyper-inflammatory response of ΔE1HK1 cells (Figure S12D), demonstrating that the physiological role for the HK1 localization switch is likely not through its effects on mitochondrial function. Additionally, in the heterozygous ΔE1HK1 mice, roughly half of the HK1 protein is attached to the mitochondria, while the rest is present in the cytoplasm (Figure S12E and S12F). If the physiological role of HK1 mitochondrial localization switch were due to its effect on mitochondrial function, the heterozygous mice would

not have displayed an increase in cytokine production or a decrease in GAPDH activity, since they still have a portion of their HK1 attached to the mitochondria. However, the heterozygous mice displayed a higher level of cytokines and a lower GAPDH activity after LPS stimulation compared to WT mice (Figure S12G and S12H), which is similar to what is observed in homozygous mice. These results support that the physiological effects of HK1 dislocation is through its cytosolic effects on GAPDH, rather than its effects on mitochondrial function.

Diabetes and aging are associated with HK1 mitochondrial dislocation and increased cytokine production

To assess the relevance of our findings in disease conditions, we next assessed whether subcellular localization of HK1 is altered in aging and diabetes, since immune cell dysregulation plays a role in these processes (Camell et al., 2019; Kwon et al., 2001; Sokolova et al., 2020). We generated high fat diet (HFD) mice, as previously described (Sawicki et al., 2018), which showed impaired glucose tolerance and increased body weight compared to mice fed a normal chow (NC) diet (Figure S13A and S13B). Importantly, BMDMs isolated from HFD mice had higher protein expression levels of cytosolic HK1 compared to NC (Figure S13C and S13D). Splenic and adipose tissue from HFD mice showed higher inflammatory mRNA levels than NC fed mice, consistent with low-grade inflammation (Figure S13E and S13F) and increased cytosolic HK1 levels (Figure S13G–S13J). Spleen tissue from aged mice (85 weeks old), also showed elevated inflammatory cytokine mRNA (Figure S13K and S13L) and increased cytosolic HK1 levels (Figure S13M and S13N).

To further support these findings, PMs isolated from HFD mice compared to NC controls displayed decreased mitochondrial localization of HK1 (Figure 7A and 7B), and decreased GAPDH activity as compared to NC cells, which was rescued with 1400W treatment (Figure 7C). HFD PMs also had higher IL-1β levels after LPS stimulation, which was rescued with 1400W treatment (Figure 7D). These findings were also recapitulated in BMDMs (Figure S13O and S13P). Additionally, HFD BMDMs displayed increased inflammatory mRNA levels, which could be reversed with iNOS inhibition (Figure S14A). We then performed S100A8 co-IP on BMDM lysates from NC and HFD mice and showed a protein interaction between S100A8 and HK1 in HFD cells (Figure S14B and S14C).

We next assessed whether our results in NC and HFD mice could be recapitulated in human peripheral blood mononuclear cells (huPBMCs) from normal control (Ctrl) and type 2 diabetes mellitus (T2DM) patients. HuPBMCs from T2DM patients displayed lower mitochondrial HK1 levels (Figure 7E and 7F) and lower GAPDH activity, which was reversed with iNOS inhibition (Figure 7G). Moreover, IL-1β levels were higher in T2DM cells as compared to controls, and this difference was abrogated after 1400W treatment (Figure 7H). Collectively, these data indicate that HK1 mitochondrial dissociation occurs in diseases of chronic-low grade inflammation in mice and humans, and that restoration of GAPDH activity with iNOS inhibition can rescue this phenotype in immune cells derived from diabetic mice and T2DM patients.

Finally, we studied the mechanism by which HK1 dislocates from the mitochondria. Unbiased proteomic analysis demonstrated that Lys15 and Lys21 residues that are within the MBD of HK1 are acetylated in the full-length protein (Figure S15A). Since the MBD of HK1 inserts into the hydrophobic mitochondrial outer membrane, we hypothesized that acetylation of the charged lysines on the HK1 MBD regulates is binding to the OMM. To test this, we made acetyl mimetic (K15Q/K21Q) and deacetyl mimetic (K15R, K21R) HK1 constructs. As expected, the K15Q/K21Q construct localizes to the mitochondria, while the K15R/K21R construct localizes mostly in the cytoplasm (Figure S15B and S15C). Cells transfected with the acetyl-mimetic constructs (K15Q/K21Q, which bind to mitochondria) displayed similar inflammatory cytokine production as controls, but the deacetyl-mimetic constructs (K15R/K21R, which do not bind to mitochondria) displayed higher inflammatory cytokine production (Figure S15D). These results support a role for HK1 MBD acetylation in regulating its subcellular localization.

We then studied a potential mechanism for acetylation of lysine residues on the HK1 MBD. Since SIRT2 is the highest upregulated sirtuin in macrophages (Ciarlo et al., 2017) we reasoned that it likely plays a role in the deacetylation of HK1. We showed that HK1 does not dislocate from the mitochondria in response to LPS in BMDMs isolated from $Sirt2^{-/-}$ mice compared to WT mice (Figure 7I and 7J). Additionally, BMDMs from $Sirt2^{-/-}$ mice displayed lower cytokine production in response to LPS (Figure 7K). These results demonstrate that the physiological role of HK1 mitochondrial binding switch on cytokine production is through its cytoplasmic effect, and that SIRT2 is a potential regulator of HK1 mitochondrial to cytosolic translocation through post-translational modification of the HK1 MBD.

DISCUSSION

Previous studies have proposed several mechanisms for HK mitochondrial binding. However, the physiologic significance of HK1 mitochondrial dissociation remains unclear. Here, we identify a mechanism by which the localization of HK1, independent of its enzymatic activity, regulates the metabolic fate of its product, G6P. These data highlight how subcellular localization of a metabolic enzyme determines the fate of its product and provides physiological significance for the mitochondrial binding of HK1. Upon dissociation from the mitochondrial outer membrane, cytosolic HK1 increases PPP flux in macrophages by enzymatic inhibition of GAPDH through iNOS-mediated nitrosylation. Although a role for GAPDH inhibition and nitrosylation in inflammation has been previously reported (Nagy and Haschemi, 2015; Baardman et al., 2018; Jia et al., 2014; Padgett and Whorton, 1995; Sanman et al., 2016), our results provide a biological context and mechanism for GAPDH regulation and link these steps to HK1 mitochondrial binding. GAPDH is a critical enzyme in glycolysis since upstream substrates can enter the PPP. Therefore, its inhibition would inhibit glycolysis while allowing the shuttling of upstream intermediates into PPP. We speculate that this mechanism serves as a means of regulating the metabolic fate of G6P into ancillary pathways off glycolysis. Since the metabolic block at GAPDH increases metabolite levels above this point, it would be interesting to investigate how other metabolic branch points (i.e., glycogenesis, one-carbon metabolism and the hexosamine pathway) are affected in other contexts.

Our data show that in the setting of conditions associated with low-grade inflammation, such as aging and diabetes, there is chronic HK1 dislocation from the mitochondria, increased production of inflammatory markers, and diminished GAPDH activity in inflammatory cells from both human and mice. These results indicate that increased cytosolic HK1 may participate in the increased inflammation observed in diabetes and aging. Thus, it may be promising to devise strategies to maintain HK1 on the mitochondria to reduce the inflammation (either low-grade or fulminant) that contributes to the negative sequelae of these and other inflammatory-associated disorders. Another interesting finding was that mice with dislocation of HK1 from the mitochondria are viable and do not present with systemic metabolic dysregulation at baseline. Instead, we observed changes in cytokine production in response to LPS. This suggests that HK1 mitochondrial binding is not required for normal embryonic development and is likely involved in the response to specific stimuli.

Our data also demonstrate a physiological role for the HK1 localization switch and delineate whether its effects on glucose metabolism and cytokine production are through a change in mitochondrial function or through cytoplasmic effects. We showed that cytosolic HK1 binds to S100A8/A9 and eventually leads to GAPDH nitrosylation and inhibition. This suggests that the effects of HK1 mitochondrial dislocation is likely through its cytosolic localization. We undertook additional experiments to further support this conclusion. First, we showed that heterozygous ΔE1HK1 mice have a similar phenotype to that of homozygous mice. Since the heterozygous mice have a portion of their HK1 attached to the mitochondria, these results suggest that the physiological effects of HK1 dislocation are likely through its cytosolic effects on GAPDH, rather than its effects on the mitochondria. Additionally, overexpression of OMPHK1 did not reverse the increase in cytokine production in BMDMs from ΔE1HK1 mice, providing further evidence that mitochondrial binding of HK1 is not required for its effects on inflammation. Furthermore, ΔE1HK1 mice had decreased survival in response to *in vivo* LPS-induced endotoxemia, which was reversed with iNOS inhibitors. In addition, *in vivo* GAPDH inhibition resulted in decreased survival when challenged with LPS induced endotoxemia, similar to ΔE1HK1 mice. Finally, iNOS inhibition reversed the effects of CLT on LPS-mediated cytokine production. Together, these results indicate that the physiological effects of HK1 mitochondrial dislocation is through its cytosolic effects, and not through changes in mitochondrial function due to HK1 dislocation from the organelle.

Our data also provide a potential mechanism for HK1 mitochondrial dissociation. Unbiased proteomic analysis demonstrated that Lys15 and Lys21 residues that are within the MBD of HK1 are acetylated in the full-length protein. Since the MBD of HK1 forms an alpha-helix that is thought to insert into the OMM, acetylation of the positively charged lysine residues would likely increase the MBD's hydrophobicity, which is needed for insertion into the hydrophobic OMM lipid membrane. Therefore, we mutated these residues, and showed that the acetyl-mimetic construct localizes to the mitochondria, while the deacetyl-mimetic construct localizes mostly to the cytoplasm. Additionally, cells transfected with the acetyl-mimetic constructs displayed similar inflammatory cytokine production to GFP-transfected cells, but the deacetyl-mimetic constructs displayed higher inflammatory cytokine production. We also show that the mechanism for this post-translational modification is likely through SIRT2.

In summary, we have shown that HK1 mitochondrial dissociation produces a metabolic block at the level of GAPDH, which increases PPP metabolism. This feature of HK1 regulation is dependent on its localization between the cytosol and mitochondria and independent of its enzymatic activity. We do not propose that the HK1 cytosolic translocation is required for pro-inflammatory cytokine production in response to LPS, but that a relative increase in cytosolic HK1 enhances inflammatory cytokine production following LPS treatment. Our data suggest that cytosolic HK1 binds to S100A8/A9, leading to S-nitrosylation of GAPDH through iNOS, and subsequent attenuation of its enzymatic activity. Therefore, HK1 subcellular localization is likely a critical modulator of glycolysis and regulates the inflammatory response in macrophages (Figure S15E).

Limitations of the Study

We used a global mouse model that lacks HK1 MBD in every organ, which raises the issue of non-tissue-specific effects of HK1 mitochondrial dissociation. However, we conducted many of our studies in isolated macrophages, which reduces the impact of other cell types on the function of these cells. Additionally, because ΔE1HK1 mice lack the HK1 mitochondrial binding domain since birth, our studies in these mice do not assess the acute effects of HK1 mitochondrial dislocation. We used CLT to address this potential issue. It is also important to note that HK1 is expressed in many cellular tissues, including the brain, and that this paper is focused on myeloid cells and does not address the role of HK1 mitochondrial binding in every tissue in the body. Finally, although we show that ΔE1HK1 mice have worse survival in the endotoxemia models, our paper does not show that the diabetic and aging models would be (at least partially) reversed with increased HK1 mitochondrial association.

STAR METHODS

RESOURCE AVAILABILITY

Lead Contact—Further information and requests for resources and reagents should be directed to and will be fulfilled by the Lead Contact, Hossein Ardehali (h-ardehali@northwestern.edu).

Materials Availability—Reagents available from the lead contact upon request.

Data and Code Availability

- Metabolomic and proteomic data have been uploaded to **to MassIVE: MSV000088901, MSV000088899**. Accession numbers are listed in the key resources table. Original western blot images and microscopy images have been deposited at Mendeley and are publicly available as of the date of publication. The DOI is listed in the key resources table
- This paper does not report original code.
- Any additional information required to reanalyze the data reported in this paper is available from the lead contact upon request.

EXPERIMENTAL MODEL AND SUBJECT DETAIL

Cell lines and culture—RAW264.7 cells were a gift from Jason A. Wertheim MD, PhD. HepG2 and HEK293T cells were obtained from ATCC. RAW264.7, HEK293T, and HepG2 cells were cultured in Dulbecco's Modified Eagle's Medium (DMEM) (Corning) supplemented with 10% FBS (Atlanta Biologicals), 2mM glutamine (HyClone), and 1mM sodium pyruvate (Corning). RAW264.7 cells were treated with 300ng/ml LPS for 4–6hrs with or without CLT (50μM).

Mouse studies—$HK1^{\Delta E1HK1/\Delta E1HK1}$ (ΔE1HK1) and $HK1^{WT/WT}$ wild type (WT) control mice were generated by the Northwestern Mutagenesis and Transgenic core. Briefly, guide RNAs (gRNAs) were designed to induce a double strand break (DSB) near the 5' ATG start codon of HK1 in exon 1, and a DNA template containing an M-DYKDDDDK (Methionine-FLAG-tag) sequence with flanking homology arms to the HK1 gene near exon 1 was introduced into fertilized zygotes and implanted into surrogate mice. Homology-directed repair (HDR) of the DSB resulted in replacement of the coding region of the HK1 MBD with the methionine-FLAG-tag sequence. Mouse genetic background is C57BL/6J. Mice were maintained in the barrier facility at Northwestern University under specific pathogen-free conditions in accordance with Federal and University guidelines and protocols approved by Institutional Animal Care and Use Committee (IACUC) with 12hr light and 12hr dark cycle, and received normal chow. Male and female mice were used at 8–12 weeks of age. We fed 4-week-old mice a HFD consisting of 60% fat, 20% protein, and 20% carbohydrates. HFD and NC diet mice were maintained on respective diets for 27 weeks. All animal studies were approved by the IACUC at Northwestern University and were performed in accordance with guidelines from the National Institutes of Health.

PM isolation and cell culture—Peritoneal macrophages were isolated from 8–10-week-old ΔE1HK1 and littermate control WT mice by peritoneal lavage as described previously (Ray and Dittel, 2010). Briefly, mice were euthanized and the peritoneal cavity was injected with PBS supplemented with 5% FBS using a 27g needle. The abdominal wall was gently agitated to dislodge peritoneal cells. Using a fresh 25g needle, the peritoneal lavage (PBS and peritoneal cells) was aspirated and collected. Cells were then centrifuged at 500g for 10min and re-suspended in 1mL of complete RPMI (Corning) supplemented with 10% FBS (Atlanta Biologicals), 2mM glutamine (HyClone), 1mM HEPES (Corning) and 1mM pyruvate (Corning). Stimulation with LPS (Invivogen) was performed the next day. 300ng/ml of LPS was given to the cells for 4–6hrs with or without the following drugs: OT (50μM), 6-AN (1mM), 1400W (50μM), or CGP3466 (50nM).

BMDM isolation and cell culture—BMDMs were isolated from ΔE1HK1 and WT mice, as previously reported (Rodriguez et al., 2019). Briefly, bone marrow was isolated from the tibia and femur of 8–10-week-old mice by puncturing one end of the femur and tibia with a 27g needle and placing it in a 0.5ml tube with a hole punched in the bottom. The 0.5ml tube containing the bone was then placed in a 1.75ml tube and centrifuged at 5,000×g for 3.5min. Bone marrow was then collected into the 1.75ml tube and resuspend in 1ml of RBC lysis buffer (abcam) for 1min and then transferred to a 50ml tube with 4ml RBC lysis buffer and incubated for 4min. Next, 35ml of PBS was added and centrifuged at 300×g for

5min and supernatant was then decanted and cell pellet was re-suspended in complete RPMI with 20ng/ml mCSF (Preprotech). Cells were counted using a hemocytometer and plated in 10cm tissue culture plates at a density of 3-million cells/plate. Cells were cultured with 20ng/mL mCSF to induce differentiation into BMDMs. Media was changed every 2 days and BMDMs were harvested by scraping on day 6 and plated in 12 well plates at a density of 1-million cells/well for mRNA extraction experiments. BMDMs were stimulated in the same manner as peritoneal macrophages (LPS dose for BMDMs was 200ng/ml).

huPBMC culture and experiments—Human peripheral blood mononuclear cells (huPBMCs) from normal control (ctrl) and type 2 diabetes mellitus (T2DM) patients were purchased from Precision for Medicine, inc (BuyPBMC). Cells were maintained in vapor phase of liquid nitrogen (−120°C). On the day of experiment, huPBMCs were thawed in 37°C water bath and gently pipetted into 10mL of complete RPMI (Corning) supplemented with 10% FBS (Atlanta Biologicals), 2mM glutamine (HyClone), 1mM HEPES (Corning) and 1mM pyruvate (Corning) and centrifuged at 500g for 10min. Media was aspirated and cells were resuspended in 1mL of complete RPMI with supplements. 100,000 cells were plated in each well of a 96 well plate and incubated overnight. Stimulation with LPS (Invivogen) was performed the next day. 200ng/ml of LPS was given to the cells for 6hrs with or without 1400W (50μM). Cells were then treated with 2mM ATP (Sigma) for 30min and media was collected for huIL-1β ELISA (DY201–05). Cellular GAPDH Activity was assessed using GAPDH activity assay kit (abcam, ab204732).

METHOD DETAILS

Generation of HK1 lentivirus gene overexpression constructs—Lentivirus C-terminal GFP-tag fusion over-expression constructs for EV, FLHK1, TrHK1, OMPHK1, FLHK1-K15R/K21R, and FLHK1-K15Q/K21Q were cloned into the pHIV-Puro vector (generated in our lab) using InFusion-HD. Lentiviral particles were produced in HEK293T cells co-transfected with pSPAX2 and pMD2.G packaging vectors using standard protocols. To generate the full-length and truncated HK1-GFP fusion plasmids, In-Fusion cloning PCR primers were designed to the first or second exon of the 2754-bp fragment from the EGFP-N3 plasmid containing FLHK1 or TrHK1. To perform the In-Fusion reaction, the PCR primers also contained overhang regions containing *Xho*I and *Bam*HI-HF restriction enzyme sites and a 15-bp homology portion to the pHIV-Puro vector to facilitate recombination. $GAPDH^{C247A}$ was generated using the mouse GAPDH-pCMV3-C-FLAG vector from SinoBiological and point mutation at Cys-247 to Ala was performed using In-Fusion cloning PCR for site-directed mutagenesis.

RNA isolation, reverse transcription and quantitative RT-PCR—RNA was isolated from cells or tissues using RNA-STAT60 (Teltest) followed by chloroform extraction and precipitation. Reverse transcription was carried out using qScript cDNA Synthesis Kit (Quanta Bio). The resulting cDNA was amplified quantitatively using PerfeCTa SYBR Green Mix (Quanta Bio) on a 7500 Fast Real-time PCR System (Applied Biosystems). The relative gene expression was determined using differences in Ct values between gene of interest and house-keeping control genes. Complete list of primers can be found in **Reagents table**.

Gene downregulation—siRNAs against mouse *s100A8, 6PGD,* and *iNOS* (Dharmacon) were transfected using Dharmafect I Transfection Reagent (Dharmacon) according to the manufacturer's protocols. We used siRNA concentrations of 25nM to achieve adequate knockdown. DharmaFECT reagent was used as per manufacturer's recommended concentration for 6, 12, and 24 well plating. siRNA and DharmaFECT were mixed in serum-free media and incubated for 5min at room-temperature and then mixed together with gentle tapping for 20min. The mix was then added dropwise to plates containing complete media and cells were incubated overnight. The next day, siRNA-media mix was removed and fresh complete media was added.

Western blots—Cells and tissue were lysed in radio-immunoprecipitation assay (RIPA) buffer supplemented with 1× protease inhibitor (G-Bioscience). Protein concentration in samples was determined using the BCA Protein Quantification Kit (Pierce). Equal amounts of protein were loaded onto a tris-glycine polyacrylamide gel (Life Technologies) and transferred to a nitrocellulose membrane. After blocking with tris-buffered saline containing 0.05% Tween 20 (DOT Scientific Inc) and 5% BSA, the membrane was incubated with primary antibody against proteins of interest. A complete list of antibodies is included in **Reagents table**. For visualization of low molecular weight protein, S100A8, samples were loaded and run on 16% tricine protein gels (Thermo-Fischer) (Schägger, 2006). The Tricine-SDS-PAGE gels were run using an anode (10× buffer, 1M Tris, 0.225M HCl, pH 8.9) and cathode (10× buffer, 1M Tris, 1M Tricine, 1% SDS, pH ~8.25) buffer system. Western blot densitometry was performed using Fiji/ImageJ *Gel analyzer* macro (Schindelin et al., 2012).

Confocal imaging—Glass-bottom confocal dishes (35 mm; VWR) were coated with 60nM fibronectin (Sigma-Aldrich), diluted in 0.1% gelatin overnight. The coated confocal dishes were washed twice with PBS before cells were plated. BMDMs (100,000 cells/well), PMs (100,000 cells/well), HepG2 (50,000 cells/well), or RAW264.7 (50,000 cells/well) cells were plated in their respective growth media (complete DMEM or RPMI) and allowed to settle overnight before immunofluorescence (IF) staining. For fixed cell immunofluorescence (IF), cells were plated in 6-well plates (Corning) containing 15mm glass coverslips (Fisher-Scientific) coated in gelatin and fibronectin. Prior to fixation, growth media was removed, and cells were washed 2× with PBS. Cells were fixed with 1ml of ice-cold 4% formaldehyde for 10min at room temperature (4% formaldehyde prepared from 16% stock and diluted in PBS). After cells were fixed, plates were washed with PBS 2× and permeabilized with 0.3% triton-X-100 in PBS for 10min at room temperature. Then, cells were blocked with 10% FBS/PBS for 1hr at room temperature and subsequently treated with primary antibody diluted in 10% FBS/PBS solution overnight. The next day, secondary antibody was diluted in 10% FBS/PBS at 1:1000 and incubated for 2hrs at room temperature. Cells were then washed 3× with PBS and mounted on glass slides (Fisher-Scientific) using ProLong Gold Antifade Mountant with DAPI and imaged using confocal microscope. HK1 antibody diluted at 1:100, ATP Synthase-beta (ATP5B) Monoclonal-Alexa Fluor 555 antibody diluted at (1:200), and MitoTracker Deep Red FM (1μM). All images were acquired on a Zeiss LSM 510 Meta confocal microscope. Images were quantified using ImageJ.

TMRE colocalization—Media was removed from HepG2 cells overexpressing EV, FLHK1, or TrHK1. Cells were washed with PBS and confocal buffer was added (25mM D-glucose, 1.8 mM CaCl2, 2.5 mM KCl, 140 mM NaCl, 2 mM sodium pyruvate, 2 mM glutamine, 20 mM HEPES, pH 7.5, 1 mM MgCl2). Cells were stained with 5nM TMRE (for mitochondrial stain) for 20min and then washed with PBS before fresh confocal buffer was added. TMRE (red channel) and GFP (green channel) signals were analyzed for colocalization using ImageJ (FIJI) Coloc-2 function to determine Pearson correlation coefficient between green and red channel for confocal images.

^{13}Carbon glucose tracing and steady-state metabolomics—Cultured BMDMs or HepG2 cells were treated with $^{13}C_6$-glucose or $^{13}C_{1-2}$-glucose for 4hrs ± LPS (200ng/ml). Mass-spectrometry and metabolite identification were performed on 80% methanol & 20% ultrapure water extracted metabolites. Whole brain tissues were harvested from mice and immediately flash frozen in liquid nitrogen until harvested for metabolites using 80% methanol & 20% ultrapure water extraction protocol. Metabolomics services were performed by the Metabolomics Core Facility at Robert H. Lurie Comprehensive Cancer Center of Northwestern University. Samples were analyzed by High-Performance Liquid Chromatography and High-Resolution Mass Spectrometry and Tandem Mass Spectrometry (HPLC-MS/MS). The system consisted of a Thermo Q-Exactive in line with an electrospray source and an Ultimate3000 (Thermo) series HPLC consisting of a binary pump, degasser, and auto-sampler outfitted with an Xbridge Amide column (Waters; dimensions of 4.6 mm × 100 mm and a 3.5 μm particle size). The mobile phase A contained 95% (vol/vol) water, 5% (vol/vol) acetonitrile, 20 mM ammonium hydroxide, 20 mM ammonium acetate, pH = 9.0; B was 100% Acetonitrile. The gradient was as following: 0min, 15% A; 2.5min, 30% A; 7min, 43% A; 16min, 62% A; 16.1–18min, 75% A; 18–25min, 15% A with a flow rate of 400 μL/min. The capillary of the ESI source was set to 275 °C, with sheath gas at 45 arbitrary units, auxiliary gas at 5 arbitrary units and the spray voltage at 4.0 kV. In positive/negative polarity switching mode, an m/z scan range from 70 to 850 was chosen and MS1 data was collected at a resolution of 70,000. The automatic gain control (AGC) target was set at 1 × 106 and the maximum injection time was 200 ms. The top 5 precursor ions were subsequently fragmented, in a data-dependent manner, using the higher energy collisional dissociation (HCD) cell set to 30% normalized collision energy in MS2 at a resolution power of 17,500. The sample volumes of 10μl were injected. Data acquisition and analysis were carried out by Xcalibur 4.0 software and Tracefinder 2.1 software, respectively (both from Thermo Fisher Scientific).

Glucose uptake assay—2-NBDG glucose uptake assay of LPS-activated BMDMs from WT and ΔE1HK1 mice was performed based on previous reports (Alonso-Castro and Salazar-Olivo, 2008). Briefly, cells were cultured overnight in 96 well plates and treated the next day with 300μM 2NBDG for 1hr. Cells were then washed 3× with PBS, re-suspended in RIPA buffer, and imaged in a fluorescent plate reader.

Extracellular IL-1β western blot—BMDMs were stimulated with O5:B55 LPS (Invivogen) for 6hrs with addition of 2mM ATP (Sigma) for 30min to activate the cleavage of pro-IL-1β (35kDa) to cleaved-IL-1β (17kDa). Cell supernatant was collected

and analyzed by ELISA according to manufacturer's instructions for IL-1β (DY401), IL-6 (DY406), and TNFα (DY410). Briefly, highly absorbent 96 well plates were used to bind the capture antibody (IL-6, TNFα, or IL-1β) which was diluted in PBS and left overnight to adhere to the 96 well plate. The next day, the plate was washed 3 times with wash buffer (PBS, 0.05% Tween20). Samples were then diluted in reagent dilution buffer (PBS, 1% BSA, 0.5X Azide, stored at 4°C), added to the plate and incubated for 2hrs. The plate was washed 3× with wash buffer and incubated for 2hrs with detection antibody, which was diluted in reagent dilution buffer. The plate was washed 3× with wash buffer and the fluorescence reaction was performed using Streptavidin-HRP-based reaction provided by the ELISA kit.

S-nitrosylation western blot of GAPDH immunoprecipitation—GAPDH immunoprecipitation of HepG2 and BMDM cells was performed and nitrosylated cysteines were replaced by covalent binding of TMT using Pierce S-Nitrosylation western blot kit according to manufactures protocol. Briefly, free cysteines were blocked with MMTS reagent, and lysates were treated with iodoTMT/ascorbate to induce replacement of unstable S-NO with stable S-TMT moiety. Western blot was then run on the TMT-replaced lysates and probed with GAPDH (dilution 1:8,000) and anti-TMT (dilution 1:1000).

Seahorse assay—The day before the assay, the Seahorse cartridge was placed in the XF calibrant and incubated overnight at 37°C. On the day of the assay, cells were seeded into the Seahorse 96-well plate at 15,000 cells/80μl per well for HepG2 cells or 100,000 cells/80μl per well for BMDMs. The plates were incubated at RT for 1hr in glucose free complete DMEM or RPMI without bicarbonate or phenol-red to allow even distribution of cells across the well floor. Before placing the sample plates in the Seahorse XF96 Analyzer, media volume was adjusted to 175μl in each well. 11mM or 25mM glucose for HepG2 cells or BMDMs respectively, 2μM Oligomycin, 10μM CCCP, and 2μM 2DG, were diluted in DMEM and injected sequentially into each well, following the standard Seahorse protocol. For acute injection of LPS, the first port of the drug cartridge was replaced with LPS at 200ng/ml.

Endotoxin-induced model of sepsis—LPS-induced sepsis model in mice was approved by Northwestern University Institutional Animal Care and Use Committee. For short term LPS-induced cytokine quantification, C57/Bl6 mice (aged 10–12 weeks) were treated intraperitoneally with or without 1400W (10mg/kg) for 2hrs prior to intraperitoneal injection with ultrapure O5:B55 LPS from Invivogen (15mg/kg) for 4hrs. Whole blood samples were harvested via cardiac puncture after mice were euthanized. Cytokine production in serum from whole blood was measured using the Mouse IL-1β (DY401), IL-6 (DY406), and TNFα (DY410) ELISAs from R&D. For survival studies, Crude O5:B55 LPS (Sigma) was administrated intraperitoneally at a sub-lethal dose of 15 mg/kg and mice were monitored over 72hrs, every 2–4hrs for survival and signs of deterioration to determine humane endpoints (Shrum et al., 2014).

Commercial assay kits—The following kits were used according to the manufacturer's instructions: Promega NADP/NADPH quantification kit (G9081) and NAD/NADPH

quantification kit (G9071); Glyceraldehyde-3-Phosphate Dehydrogenase Activity Assay kit (abcam, ab204732); ELISAs for IL-1β (DY401), IL-6 (DY410), and TNFα (DY406).

CBC and WBC from whole blood—A HEMEVET blood cell analyzer was used on whole blood from mice using mouse standard blood as a control for comparing readouts.

Co-immunoprecipitation—Anti-HK1 (MB101347-T38–1) and anti-s100A8 (MB11138-R203–20) magnetic bead IP kits (Sino Biological) were used to IP HK1 or s100A8 from BMDMs. BMDMs were plated in 15cm culture dishes and lysed using NP40 cell lysis buffer (Sino Biological-provided in kit) and sonicated for 5 pulses for 1sec each. Lysate was centrifuged at 8,000×g and supernatant was collected in a fresh tube. 50μL of HK1-magnetic beads was added to a fresh 1.7mL tube and washed with 150μL 1×TBS (10×TBS: 60.6g Tris, 87.6g NaCl, 1M HCl, 7.5pH) with 0.5% Tween-20 (DOT Scientific Inc) and beads were precipitated with magnetic separator (Sino Biological-provided in kit). 1,000ug of lysate from ΔE1HK1 and WT BMDMs was added to the precipitated magnetic HK1 beads and incubated overnight at 4° on a rotator. The next day, beads were magnetically precipitated and washed 3× with 1×TBST. Bound protein from precipitated beads was eluted using acidity elution buffer (Sino Biological, provided in kit) and western blot analysis was performed.

Mass spectrometry—HepG2 cells were plated to confluency on 15cm dishes before scraped in 10-mL PBS and collected into 15mL conical tube. Cells were centrifuged at 500×g for 15min at 4°C. Supernatant was aspirated, and cell pellet was re-suspended in 300μL co-IP lysis buffer (100mM HEPES-pH 7.7, 250mM KCl, 2mM MgCl2, 2mM EDTA, 10% glycerol, 1% digitonin) and transferred to 1.7mL tubes. The lysate was then sonicated for 5 pulses of 1sec each and incubated on ice for 30min. Lysates were then centrifuged at 16,000×g for 15min and supernatant was collected in fresh 1.7mL tube. Protein quantification was performed using BCA Protein Quantification Kit (Pierce) and 2,000μg of protein was used for co-IP. Co-IP was performed using GFP-Trap-Agarose beads (Chromotek) according to manufacturer's protocol. Eluted samples were given to the Northwestern Proteomics Core using the 100-minute gradient tandem mass spectrometry Orbitrap. The protein sample was analyzed by nanocapillary LC-MS using 100mm × 75μm ID PLRP-S column in-line with an Orbitrap Elite. MS method involved 1) FT scan, m/z 400–2,000, 120,000 resolving power and 2) data-dependent MS/MS on the top 2 peaks in each spectrum from scan event 1 using higher-energy collisional dissociation (HCD) with normalized collision energy of 25, isolation width 50 m/z, and detection of ions with resolving power of 60,000. All data were analyzed using QualBrowser, part of the Xcalibur software packaged with the ThermoFisher Orbitrap Elite.

Lactate quantification assay—Lactate quantification adapted from previous work (Gandhi et al., 2009). The lactate reporter system contained 200μmol/L Amplex red (Molecular Probes), 4 units/mL lactate oxidase (Sigma), and 0.8 units/mL horseradish peroxidase (Sigma) in 50mmol/L Tris–HCl, pH 7.4, which was deoxygenated with helium to reduce oxidation of Amplex red. The assays were incubated for 30min, followed by measurement of fluorescence at 590nm using excitation at 530nm.

Glucose-6-phosphate quantification assay—Glucose-6-phosphate (G6P) quantification assay was adapted from previous work (Zhu et al., 2009). 10μl of G6P standards and extraction samples were pipetted onto a 96-well plate and 90μl of a cocktail of 50 mM triethanolamine (pH 7.6), 1.0mM $MgCl_2$, 100μM NADP+, 10μM resazurin, 0.1U/ml G6PD, and 0.2U/ml diaphorase was added. The plate was incubated for 30min, followed by measurement of fluorescence at 590nm using excitation at 530nm.

***In vivo* metabolic studies—**For all *in vivo* metabolic studies, age-matched WT and ΔE1HK1 littermates were used. For the glucose-tolerance test (GTT), mice were fasted for 16hrs and injected intraperitoneally with a 20% dextrose (Millipore Sigma) solution in PBS at 2g/kg body weight. For the insulin-tolerance test (ITT), mice were fasted for 4hr and injected peritoneally with a 0.1 U Humulin/ml PBS solution at 0.75 U/kg body weight (Lily).

Mitochondrial and cytosolic subcellular fractionation—Mitochondrial Isolation Kit for Tissue (Pierce) was used to purify mitochondrial and cytosolic protein subcellular fractions according to the Pierce manufacturer's protocol. Briefly, this method is based on detergent extraction to produce membrane and cytosolic fractions. First, cells are permeabilized with a hypotonic buffer and disrupted effectively by Dounce homogenizer before being spun down at 1000×g. The supernatant containing the cytoplasmic fraction is placed in a separate tube. Then, the pellet containing the mitochondrial membrane fractions is resuspended in a buffer containing Tris-HCl, NaCl and mild detergent 1.5% Triton X-100. Standard western blot electrophoresis was performed as described above.

HK activity assay—HK activity was determined, as previously described (Majewski et al., 2004). In brief, cells were plated on 12cm dishes and allowed to attach overnight. The next day, cells were washed once with PBS before harvested by scraping and pelleted at 500×g for 5min. Cells were lysed by sonication, five pulses of 1sec, in 100μl homogenization buffer: 0.2% Triton X-100, 0.5mM EGTA, 10mM D-(+)-glucose, 11.1mM monothioglycerol, 45mM Tris-HCl (pH 8.2), and 50mM KH_2PO_4. After sonication, lysates were centrifuged at 7,000×g for 5min. HK activity was determined by the whole-cell lysate's ability to phosphorylate glucose over 2min in an assay mixture with final concentrations of 50mM triethanolamine chloride, 7.5mM MgCl2, 0.5mM EGTA, 1 mM monothioglycerol, 0.5 to 25mM glucose, 6.6mM ATP, 0.5mg/mL NADP, and 0.5U/mL G6PDH, pH 8.5. G6P formation was measured indirectly by NADPH production from G6PDH by measuring absorbance at 340nm on a spectrophotometer and was normalized to protein concentration as determined by BCA protein assay kit (Fisher Scientific).

QUANTIFICATION AND STATISTICAL ANALYSIS

Data are presented as mean ± SD, unless otherwise stated. For a two-group comparison unpaired two-tailed Student's t-tests was used. For data with multiple groups (>2) or multiple treatments a one- or two-way ANOVA was used as indicated followed by Tukey's post-hoc test to determine p-values for individual comparisons. No statistical methods were used to predetermine sample size. All statistical analysis was performed using Graphpad Prism 8.0. $p < 0.05$ was considered statistically significant and is presented as * $p < 0.05$,

** $p < 0.01$, *** $p < 0.001$, **** $p < 0.0001$, or ns = not significant). Survival experiment was performed in Prism 8 using comparison of survival curves with Log-rank (Mantel-Cox) test. For *in vivo* experiments, animals were assigned to experimental groups using simple randomization, without investigator blinding. Hierarchical clustering and heatmaps for metabolomics data were generated using MetaboAnalyst 4.0 statistical software (Chong et al., 2019).

Supplementary Material

Refer to Web version on PubMed Central for supplementary material.

ACKNOWELEDGEMENTS

We would like to thank Meng Shang and Eric Xia for managing our mouse colony and genotyping the mice used in this study. Thanks to Peng Gao from the Metabolomics Core Facility at Robert H. Lurie Comprehensive Cancer Center of Northwestern University for performing metabolomics mass-spectrometry for our metabolomics experiments. We thank Young Ah Goo from the Northwestern University Proteomics Center of Excellence for running the mass-spectrometry for our proteomics experiments. We thank Lynn Doglio and Pei-Ken from the Northwestern Transgenic and Targeted Mutagenesis for generating the ΔE1HK1 mice. Graphical abstract art generated using modified images from Smart Servier Medical Art (Les Laboratoires Servier). Funding for this work was provided through NRSA 5F31HL132552-04 awarded to A.D., and NHLBI HL127646, HL140973, and HL138982 awarded to H.A. B.T.L. is supported by the National Institutes of Health under award number, R01DK104927 and Department of Veterans Affairs, Veterans Health Administration, Office of Research and Development, VA merit (Grant no. 1I01BX003382).

Funding Acquisition: A.D., and H.A.

REFERENCES

Adeva-Andany MM, Perez-Felpete N, Fernandez-Fernandez C, Donapetry-Garcia C, and Pazos-Garcia C (2016). Liver glucose metabolism in humans. Biosci. Rep. 36, e00416–e00416. [PubMed: 27707936]

Aflalo C, and Azoulay H (1998). Binding of Rat Brain Hexokinase to Recombinant Yeast Mitochondria: Effect of Environmental Factors and the Source of Porin. J. Bioenerg. Biomembr. 30, 245–255. [PubMed: 9733091]

Alonso-Castro AJ, and Salazar-Olivo LA (2008). The anti-diabetic properties of Guazuma ulmifolia Lam are mediated by the stimulation of glucose uptake in normal and diabetic adipocytes without inducing adipogenesis. J. Ethnopharmacol. 118, 252–256. [PubMed: 18487028]

Andrejeva G, and Rathmell JC (2017). Similarities and Distinctions of Cancer and Immune Metabolism in Inflammation and Tumors. Cell Metab. 26, 49–70. [PubMed: 28683294]

Azoulay-Zohar H, Israelson A, Abu-Hamad S, and Shoshan-Barmatz V (2004). In self-defence: hexokinase promotes voltage-dependent anion channel closure and prevents mitochondria-mediated apoptotic cell death. Biochem. J. 377, 347–355. [PubMed: 14561215]

Baardman J, Verberk SGS, Prange KHM, van Weeghel M, van der Velden S, Ryan DG, Wüst RCI, Neele AE, Speijer D, Denis SW, et al. (2018). A Defective Pentose Phosphate Pathway Reduces Inflammatory Macrophage Responses during Hypercholesterolemia. Cell Rep. 25, 2044–2052.e5. [PubMed: 30463003]

Bantug GR, Fischer MG, Grählert J, Balmer ML, Unterstab G, Develioglu L, Steiner R, Zhang L, da Costa ASH, Gubser PM, et al. (2018). Mitochondria–ER contact sites are immunometabolic hubs that orchestrate the rapid recall response of memory CD8+ T cells. Immunity 48, 542–555.e6. [PubMed: 29523440]

Bell GI, Burant CF, Takeda J, and Gould GW (1993). Structure and function of mammalian facilitative sugar transporters. J. Biol. Chem. 268, 19161–19164. [PubMed: 8366068]

Camell CD, Günther P, Lee A, Goldberg EL, Spadaro O, Youm Y-H, Bartke A, Hubbard GB, Ikeno Y, Ruddle NH, et al. (2019). Aging Induces an Nlrp3 Inflammasome-Dependent Expansion of Adipose B Cells That Impairs Metabolic Homeostasis. Cell Metab. 0.

Cheng S-C, Quintin J, Cramer RA, Shepardson KM, Saeed S, Kumar V, Giamarellos-Bourboulis EJ, Martens JHA, Rao NA, Aghajanirefah A, et al. (2014). mTOR- and HIF-1α-mediated aerobic glycolysis as metabolic basis for trained immunity. Science 345, 1250684. [PubMed: 25258083]

Chong J, Wishart DS, and Xia J (2019). Using MetaboAnalyst 4.0 for Comprehensive and Integrative Metabolomics Data Analysis. Curr. Protoc. Bioinforma. 68, e86.

Ciarlo E, Heinonen T, Théroude C, Herderschee J, Mombelli M, Lugrin J, Pfefferlé M, Tyrrell B, Lensch S, Acha-Orbea H, et al. (2017). Sirtuin 2 Deficiency Increases Bacterial Phagocytosis by Macrophages and Protects from Chronic Staphylococcal Infection. Front. Immunol. 8, 1037. [PubMed: 28894448]

Everts B, Amiel E, Huang SC-C, Smith AM, Chang C-H, Lam WY, Redmann V, Freitas TC, Blagih J, van der Windt GJW, et al. (2014). TLR-driven early glycolytic reprogramming via the kinases TBK1-IKKε supports the anabolic demands of dendritic cell activation. Nat. Immunol. 15, 323–332. [PubMed: 24562310]

Fiek C, Benz R, Roos N, and Brdiczka D (1982). Evidence for identity between the hexokinase-binding protein and the mitochondrial porin in the outer membrane of rat liver mitochondria. Biochim. Biophys. Acta 688, 429–440. [PubMed: 6285967]

Garaude J, Acín-Pérez R, Martínez-Cano S, Enamorado M, Ugolini M, Nistal-Villán E, Hervás-Stubbs S, Pelegrín P, Sander LE, Enríquez JA, et al. (2016). Mitochondrial respiratory-chain adaptations in macrophages contribute to antibacterial host defense. Nat. Immunol. 17, 1037–1045. [PubMed: 27348412]

Golshani-Hebroni SG, and Bessman SP (1997). Hexokinase binding to mitochondria: a basis for proliferative energy metabolism. J. Bioenerg. Biomembr. 29, 331–338. [PubMed: 9387093]

Gould GW, and Holman GD (1993). The glucose transporter family: structure, function and tissue-specific expression. Biochem. J. 295, 329–341. [PubMed: 8240230]

Halestrap AP, Pereira GC, and Pasdois P (2015). The role of hexokinase in cardioprotection – mechanism and potential for translation. Br. J. Pharmacol. 172, 2085–2100. [PubMed: 25204670]

Ham M, Lee J-W, Choi AH, Jang H, Choi G, Park J, Kozuka C, Sears DD, Masuzaki H, and Kim JB (2013). Macrophage Glucose-6-Phosphate Dehydrogenase Stimulates Proinflammatory Responses with Oxidative Stress. Mol. Cell. Biol. 33, 2425–2435. [PubMed: 23572562]

Huang J-B, Kindzelskii AL, and Petty HR (2002). Hexokinase translocation during neutrophil activation, chemotaxis, and phagocytosis: disruption by cytochalasin D, dexamethasone, and indomethacin. Cell. Immunol. 218, 95–106. [PubMed: 12470617]

Hughes MM, and O'Neill LAJ (2018). Metabolic regulation of NLRP3. Immunol. Rev. 281, 88–98. [PubMed: 29247992]

Hwang J-S, Kwon M-Y, Kim K-H, Lee Y, Lyoo IK, Kim JE, Oh E-S, and Han I-O (2017). Lipopolysaccharide (LPS)-stimulated iNOS Induction Is Increased by Glucosamine under Normal Glucose Conditions but Is Inhibited by Glucosamine under High Glucose Conditions in Macrophage Cells. J. Biol. Chem. 292, 1724–1736. [PubMed: 27927986]

Jha AK, Huang SC-C, Sergushichev A, Lampropoulou V, Ivanova Y, Loginicheva E, Chmielewski K, Stewart KM, Ashall J, Everts B, et al. (2015). Network Integration of Parallel Metabolic and Transcriptional Data Reveals Metabolic Modules that Regulate Macrophage Polarization. Immunity 42, 419–430. [PubMed: 25786174]

Jia J, Arif A, Terenzi F, Willard B, Plow EF, Hazen SL, and Fox PL (2014). Target-selective Protein S-Nitrosylation by Sequence Motif Recognition. Cell 159, 623–634. [PubMed: 25417112]

Kwon HJ, Sung BK, Kim JW, Lee JH, Kim ND, Yoo MA, Kang HS, Baek HS, Bae SJ, Choi JS, et al. (2001). The effect of lipopolysaccharide on enhanced inflammatory process with age: Modulation of NF-κB. J. Am. Aging Assoc. 24, 163–171. [PubMed: 23604881]

Les Laboratoires Servier SMART.

Lindén M, Gellerfors P, and Nelson BD (1982). Pore protein and the hexokinase-binding protein from the outer membrane of rat liver mitochondria are identical. FEBS Lett. 141, 189–192. [PubMed: 6178620]

Lobas MA, Tao R, Nagai J, Kronschläger MT, Borden PM, Marvin JS, Looger LL, and Khakh BS (2019). A genetically encoded single-wavelength sensor for imaging cytosolic and cell surface ATP. Nat. Commun. 10, 711. [PubMed: 30755613]

Majewski N, Nogueira V, Robey RB, and Hay N (2004). Akt Inhibits Apoptosis Downstream of BID Cleavage via a Glucose-Dependent Mechanism Involving Mitochondrial Hexokinases. Mol. Cell. Biol. 24, 730–740. [PubMed: 14701745]

Manfredi G, Yang L, Gajewski CD, and Mattiazzi M (2002). Measurements of ATP in mammalian cells. Methods 26, 317–326. [PubMed: 12054922]

Martinez FO, Gordon S, Locati M, and Mantovani A (2006). Transcriptional profiling of the human monocyte-to-macrophage differentiation and polarization: new molecules and patterns of gene expression. J. Immunol. Baltim. Md 1950 177, 7303–7311.

Mi H, Muruganujan A, Ebert D, Huang X, and Thomas PD (2019). PANTHER version 14: more genomes, a new PANTHER GO-slim and improvements in enrichment analysis tools. Nucleic Acids Res. 47, D419–D426. [PubMed: 30407594]

Middleton RJ (1990). Hexokinases and glucokinases. Biochem. Soc. Trans. 18, 180–183. [PubMed: 2199258]

Moon J-S, Hisata S, Park M-A, DeNicola GM, Ryter SW, Nakahira K, and Choi AMK (2015). mTORC1 induced HK1-dependent glycolysis regulates NLRP3 inflammasome activation. Cell Rep. 12, 102–115. [PubMed: 26119735]

Mueckler M (1994). Facilitative glucose transporters. Eur. J. Biochem. 219, 713–725. [PubMed: 8112322]

Nagy C, and Haschemi A (2015). Time and Demand are Two Critical Dimensions of Immunometabolism: The Process of Macrophage Activation and the Pentose Phosphate Pathway. Front. Immunol. 6.

Nishizawa T, Kanter JE, Kramer F, Barnhart S, Shen X, Vivekanandan-Giri A, Wall VZ, Kowitz J, Devaraj S, O'Brien KD, et al. (2014). Testing the Role of Myeloid Cell Glucose Flux in Inflammation and Atherosclerosis. Cell Rep. 7, 356–365. [PubMed: 24726364]

O'Neill LAJ, and Pearce EJ (2016). Immunometabolism governs dendritic cell and macrophage function. J. Exp. Med. 213, 15–23. [PubMed: 26694970]

Padgett CM, and Whorton AR (1995). S-nitrosoglutathione reversibly inhibits GAPDH by S-nitrosylation. Am. J. Physiol.-Cell Physiol. 269, C739–C749.

Pasdois P, Parker JE, and Halestrap AP (2013). Extent of Mitochondrial Hexokinase II Dissociation During Ischemia Correlates With Mitochondrial Cytochrome c Release, Reactive Oxygen Species Production, and Infarct Size on Reperfusion. J. Am. Heart Assoc. Cardiovasc. Cerebrovasc. Dis. 2.

Pastorino JG, Shulga N, and Hoek JB (2002). Mitochondrial Binding of Hexokinase II Inhibits Bax-induced Cytochrome c Release and Apoptosis. J. Biol. Chem. 277, 7610–7618. [PubMed: 11751859]

Pavlova NN, and Thompson CB (2016). The Emerging Hallmarks of Cancer Metabolism. Cell Metab. 23, 27–47. [PubMed: 26771115]

Pearce EL, and Pearce EJ (2013). Metabolic Pathways in Immune Cell Activation and Quiescence. Immunity 38, 633–643. [PubMed: 23601682]

Printz RL, Koch S, Potter LR, O'Doherty RM, Tiesinga JJ, Moritz S, and Granner DK (1993). Hexokinase II mRNA and gene structure, regulation by insulin, and evolution. J. Biol. Chem. 268, 5209–5219. [PubMed: 8444897]

Printz RL, Ardehali H, Koch S, and Granner DK (1995). Human Hexokinase II mRNA and Gene Structure. Diabetes 44, 290–294. [PubMed: 7883116]

Printz RL, Osawa H, Ardehali H, Koch S, and Granner DK (1997). Hexokinase II gene: structure, regulation and promoter organization. Biochem. Soc. Trans. 25, 107–112. [PubMed: 9056853]

Puleston DJ, Villa M, and Pearce EL (2017). Ancillary Activity: Beyond Core Metabolism in Immune Cells. Cell Metab. 26, 131–141. [PubMed: 28683280]

Pusec CM, De Jesus A, Khan MW, Terry AR, Ludvik AE, Xu K, Giancola N, Pervaiz H, Daviau Smith E, Ding X, et al. (2019). Hepatic HKDC1 Expression Contributes to Liver Metabolism. Endocrinology 160, 313–330. [PubMed: 30517626]

Ray A, and Dittel BN (2010). Isolation of Mouse Peritoneal Cavity Cells. J. Vis. Exp.

Rodriguez AE, Ducker GS, Billingham LK, Martinez CA, Mainolfi N, Suri V, Friedman A, Manfredi MG, Weinberg SE, Rabinowitz JD, et al. (2019). Serine Metabolism Supports Macrophage IL-1β Production. Cell Metab. 29, 1003–1011.e4. [PubMed: 30773464]

Rose IA, and Warms JV (1967a). Mitochondrial hexokinase. Release, rebinding, and location. J. Biol. Chem. 242, 1635–1645. [PubMed: 4225734]

Rose IA, and Warms JVB (1967b). Mitochondrial Hexokinase RELEASE, REBINDING, AND LOCATION. J. Biol. Chem. 242, 1635–1645. [PubMed: 4225734]

Sancho D, Enamorado M, and Garaude J (2017). Innate Immune Function of Mitochondrial Metabolism. Front. Immunol. 8.

Sanman LE, Qian Y, Eisele NA, Ng TM, van der Linden WA, Monack DM, Weerapana E, and Bogyo M (2016). Disruption of glycolytic flux is a signal for inflammasome signaling and pyroptotic cell death. ELife 5, e13663. [PubMed: 27011353]

Sawicki KT, Chang H-C, Shapiro JS, Bayeva M, De Jesus A, Finck BN, Wertheim JA, Blackshear PJ, and Ardehali H (2018). Hepatic tristetraprolin promotes insulin resistance through RNA destabilization of FGF21. JCI Insight 3.

Schägger H (2006). Tricine–SDS-PAGE. Nat. Protoc. 1, 16–22. [PubMed: 17406207]

Schindelin J, Arganda-Carreras I, Frise E, Kaynig V, Longair M, Pietzsch T, Preibisch S, Rueden C, Saalfeld S, Schmid B, et al. (2012). Fiji: an open-source platform for biological-image analysis. Nat. Methods 9, 676–682. [PubMed: 22743772]

Sen S, Kaminiski R, Deshmane S, Langford D, Khalili K, Amini S, and Datta PK (2015). Role of hexokinase-1 in the survival of HIV-1-infected macrophages. Cell Cycle Georget. Tex 14, 980–989.

Shoshan-Barmatz V, Zakar M, Rosenthal K, and Abu-Hamad S (2009). Key regions of VDAC1 functioning in apoptosis induction and regulation by hexokinase. Biochim. Biophys. Acta BBA - Bioenerg. 1787, 421–430.

Shoshan-Barmatz V, De Pinto V, Zweckstetter M, Raviv Z, Keinan N, and Arbel N (2010). VDAC, a multi-functional mitochondrial protein regulating cell life and death. Mol. Aspects Med. 31, 227–285. [PubMed: 20346371]

Shrum B, Anantha RV, Xu SX, Donnelly M, Haeryfar SM, McCormick JK, and Mele T (2014). A robust scoring system to evaluate sepsis severity in an animal model. BMC Res. Notes 7, 233. [PubMed: 24725742]

Sokolova M, Yang K, Hansen SH, Louwe MC, Kummen M, Hov JER, Sjaastad I, Berge RK, Halvorsen B, Aukrust P, et al. (2020). NLRP3 inflammasome deficiency attenuates metabolic disturbances involving alterations in the gut microbial profile in mice exposed to high fat diet. Sci. Rep. 10, 21006. [PubMed: 33273482]

Stienstra R, Netea-Maier RT, Riksen NP, Joosten LAB, and Netea MG (2017). Specific and Complex Reprogramming of Cellular Metabolism in Myeloid Cells during Innate Immune Responses. Cell Metab. 26, 142–156. [PubMed: 28683282]

Sui D, and Wilson JE (1997). Structural Determinants for the Intracellular Localization of the Isozymes of Mammalian Hexokinase: Intracellular Localization of Fusion Constructs Incorporating Structural Elements from the Hexokinase Isozymes and the Green Fluorescent Protein. Arch. Biochem. Biophys. 345, 111–125. [PubMed: 9281318]

Sun L, Shukair S, Naik TJ, Moazed F, and Ardehali H (2008). Glucose Phosphorylation and Mitochondrial Binding Are Required for the Protective Effects of Hexokinases I and II. Mol. Cell. Biol. 28, 1007–1017. [PubMed: 18039843]

Tanaka T, Saotome M, Katoh H, Satoh T, Hasan P, Ohtani H, Satoh H, Hayashi H, and Maekawa Y (2018). Glycogen synthase kinase-3β opens mitochondrial permeability transition pore through mitochondrial hexokinase II dissociation. J. Physiol. Sci. 68, 865–871. [PubMed: 29671257]

Thomsen LL, Scott JMJ, Topley P, Knowles RG, Keerie A-J, and Frend AJ (1997). Selective Inhibition of Inducible Nitric Oxide Synthase Inhibits Tumor Growth in Vivo: Studies with 1400W, a Novel Inhibitor. Cancer Res. 57, 3300–3304. [PubMed: 9242464]

Tyson RL, Perron J, and Sutherland GR (2000). 6-Aminonicotinamide inhibition of the pentose phosphate pathway in rat neocortex. Neuroreport 11, 1845–1848. [PubMed: 10884030]

Ureta T (1982). The comparative isozymology of vertebrate hexokinases. Comp. Biochem. Physiol. B 71, 549–555. [PubMed: 7044667]

Wang J, Zhang X, Ma D, Lee W-NP, Xiao J, Zhao Y, Go VL, Wang Q, Yen Y, Recker R, et al. (2013). Inhibition of transketolase by oxythiamine altered dynamics of protein signals in pancreatic cancer cells. Exp. Hematol. Oncol. 2.

Wang MJ, Jeng KCG, and Shih PC (1999). Differential expression of inducible nitric oxide synthase gene by alveolar and peritoneal macrophages in lipopolysaccharide-hyporesponsive C3H/HeJ mice. Immunology 98, 497–503. [PubMed: 10594680]

Wang S, Song R, Wang Z, Jing Z, Wang S, and Ma J (2018). S100A8/A9 in Inflammation. Front. Immunol. 9.

Wilson JE (2003). Isozymes of mammalian hexokinase: structure, subcellular localization and metabolic function. J. Exp. Biol. 206, 2049–2057. [PubMed: 12756287]

Wolf AJ, Reyes CN, Liang W, Becker C, Shimada K, Wheeler ML, Cho HC, Popescu NI, Coggeshall KM, Arditi M, et al. (2016). Hexokinase Is an Innate Immune Receptor for the Detection of Bacterial Peptidoglycan. Cell 166, 624–636. [PubMed: 27374331]

Zhang D, Yip YM, and Li L (2016). In silico construction of HK2-VDAC1 complex and investigating the HK2 binding-induced molecular gating mechanism of VDAC1. Mitochondrion 30, 222–228. [PubMed: 27544294]

Zhang W, Wang G, Xu Z-G, Tu H, Hu F, Dai J, Chang Y, Chen Y, Lu Y, Zeng H, et al. (2019). Lactate Is a Natural Suppressor of RLR Signaling by Targeting MAVS. Cell 178, 176–189.e15. [PubMed: 31155231]

Zhu A, Romero R, and Petty HR (2009). An enzymatic fluorimetric assay for glucose-6-phosphate: application in an in vitro Warburg-like effect. Anal. Biochem. 388, 97–101. [PubMed: 19454216]

Zou C, Wang Y, and Shen Z (2005). 2-NBDG as a fluorescent indicator for direct glucose uptake measurement. J. Biochem. Biophys. Methods 64, 207–215. [PubMed: 16182371]

Highlights:

- HK1 mitochondrial dissociation results in GAPDH inhibition and increased PPP
- Cytosolic HK1 increases macrophage-mediated inflammatory cytokine production
- HK1 associates with S100A8/A9 and attenuates GAPDH activity through nitrosylation
- Diabetic and aging immune cells show cytosolic HK1 and reduced GAPDH activity

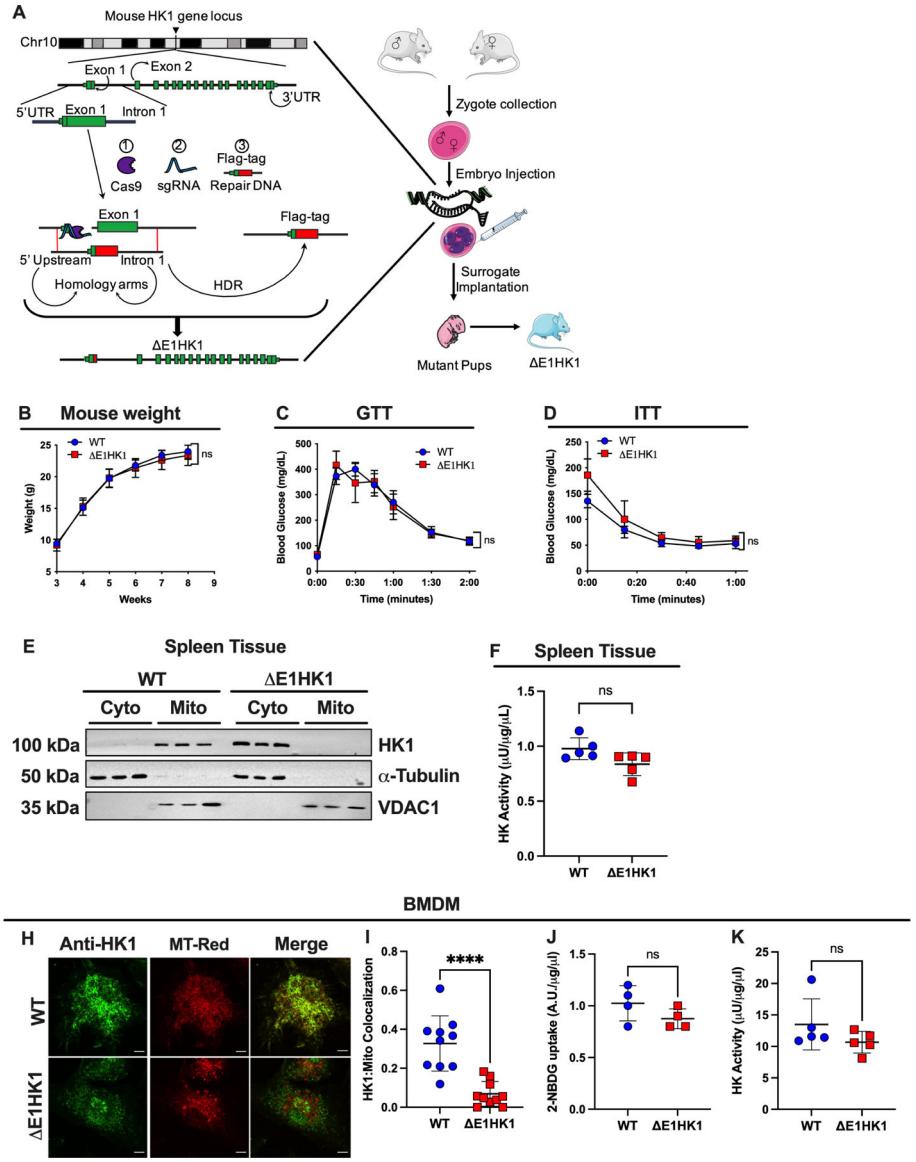

Figure 1. Deletion of HK1 MBD in mice using CRISPR-Cas9

(A) Schematic of HK1 mouse model generation using CRISPR-Cas9.

(B) Mouse weights from 3 to 8 weeks (n=5 mice per condition, repeated measures two-way ANOVA).

(C-D) Glucose tolerance test (GTT) (C) and insulin tolerance test (ITT) (D) from 10-week-old mice (n=5 mice per condition, repeated measures two-way ANOVA).

(E) Mitochondria and cytosolic protein fractionation and western blot of spleen tissue, blotted for HK1, with VDAC1 mitochondrial marker and α-tubulin cytosolic marker (n=3 mice per condition).

(F) HK activity assay normalized to total protein from spleen tissue (n=5 mice per condition, unpaired t-test).

(H) Representative immunofluorescence (IF) images probing for HK1 and mitochondria (MT-Red) in isolated BMDMs from WT and ΔE1HK1 mice.

(I) Colocalization analysis of IF images using Pearson's correlation coefficient calculated per cell between MT-Red (red) and HK1 (green) image channels (n=10 cells per condition, unpaired t-test, scale bar = 15μm).
(J) 2-NBDG glucose uptake assay normalized to total protein of LPS (200ng/ml)-activated BMDMs (n=4 mice per condition, unpaired t-test).
(K) HK activity assay normalized to total protein of LPS (200ng/ml)-activated BMDMs (n=5 mice per condition, unpaired t-test).

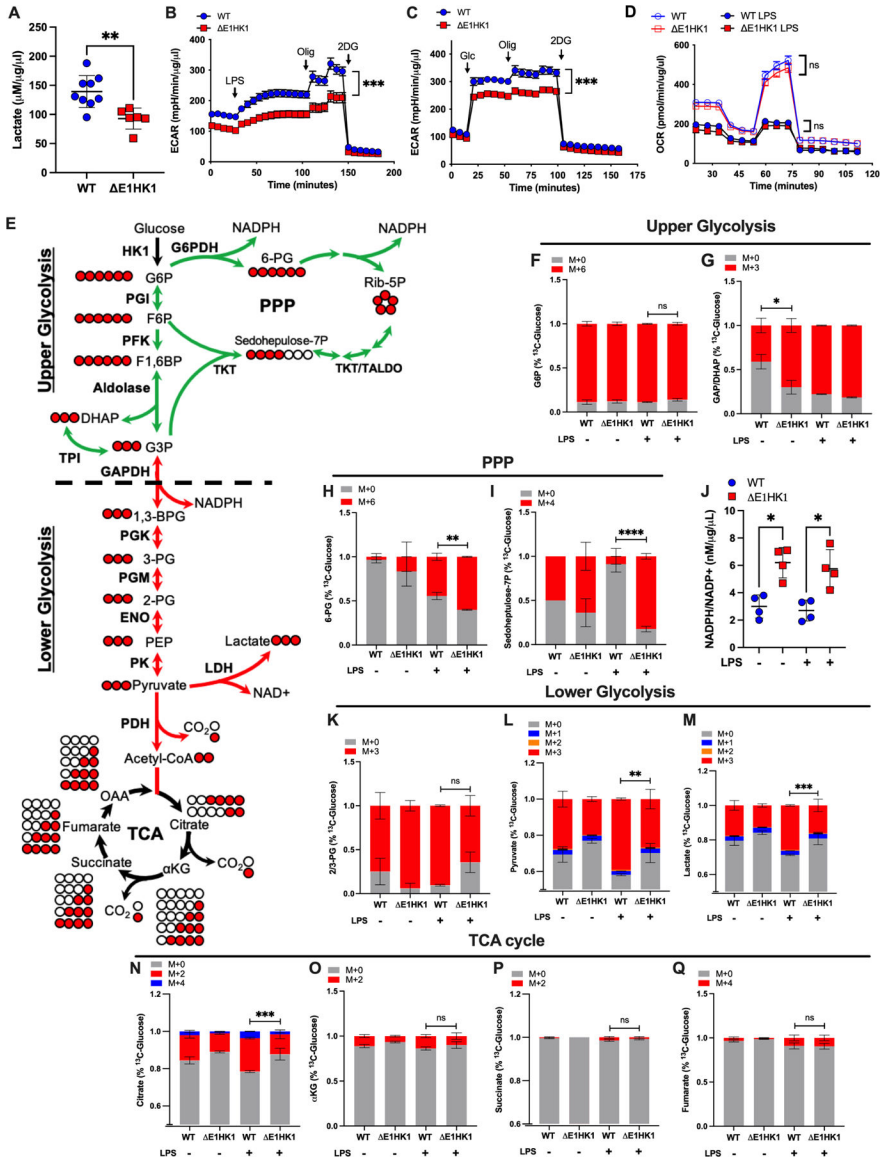

Figure 2. Loss of HK1 mitochondrial binding alters glucose metabolism and increases PPP intermediates

(A) Extracellular lactate quantification in LPS-activated BMDMs (n=6–9 mice per condition, unpaired t-test).

(B) ECAR trace of unstimulated BMDMS ± acute LPS (200ng/ml) stimulation for 2hrs (n=9 mice per condition, repeated measures two-way ANOVA, mean ± SEM).

(C) ECAR trace of BMDMS ± 5hrs LPS (200ng/ml) stimulation (n=5 mice per condition, repeated measures two-way ANOVA).

(D) OCR trace of BMDMS ± 5hrs LPS (200ng/ml) stimulation (n=5 mice per condition, repeated measures two-way ANOVA).

(E) Schematic of ^{13}C-glucose carbon labeling through glycolysis (upper and lower glycolysis), PPP, and TCA cycle. Green arrow indicates increased metabolites and red depicts reduced levels of metabolites.

(F-G) ^{13}C-glucose incorporation into upper glycolytic metabolites, G6P (E) and GAP (F), ± 4hrs LPS treatment (n=5 mice per condition, two-way ANOVA, mean ± SEM).
(H-I) ^{13}C-glucose incorporation into PPP metabolites, 6-PG (G) and sedoheptulose-7P (H), ± 4hrs LPS treatment (n=5 mice per condition, two-way ANOVA, mean ± SEM).
(J) NADPH/NADP+ ratio normalized to total protein in isolated BMDMs ±4hr LPS treatment (N=4 mice per condition, one-way ANOVA and Tukey's post-hoc test).
(K-M) ^{13}C-glucose incorporation into lower glycolytic metabolites, 2/3-PG (J), pyruvate (K), and lactate (L), ± 4hrs LPS treatment (n=5 mice per condition, two-way ANOVA, mean ± SEM).
(N-Q) ^{13}C-glucose incorporation into TCA metabolites, citrate (M), αKG (N), succinate (O), and fumarate (P) ± 4hrs LPS treatment (n=5 mice per condition, two-way ANOVA, mean ± SEM).

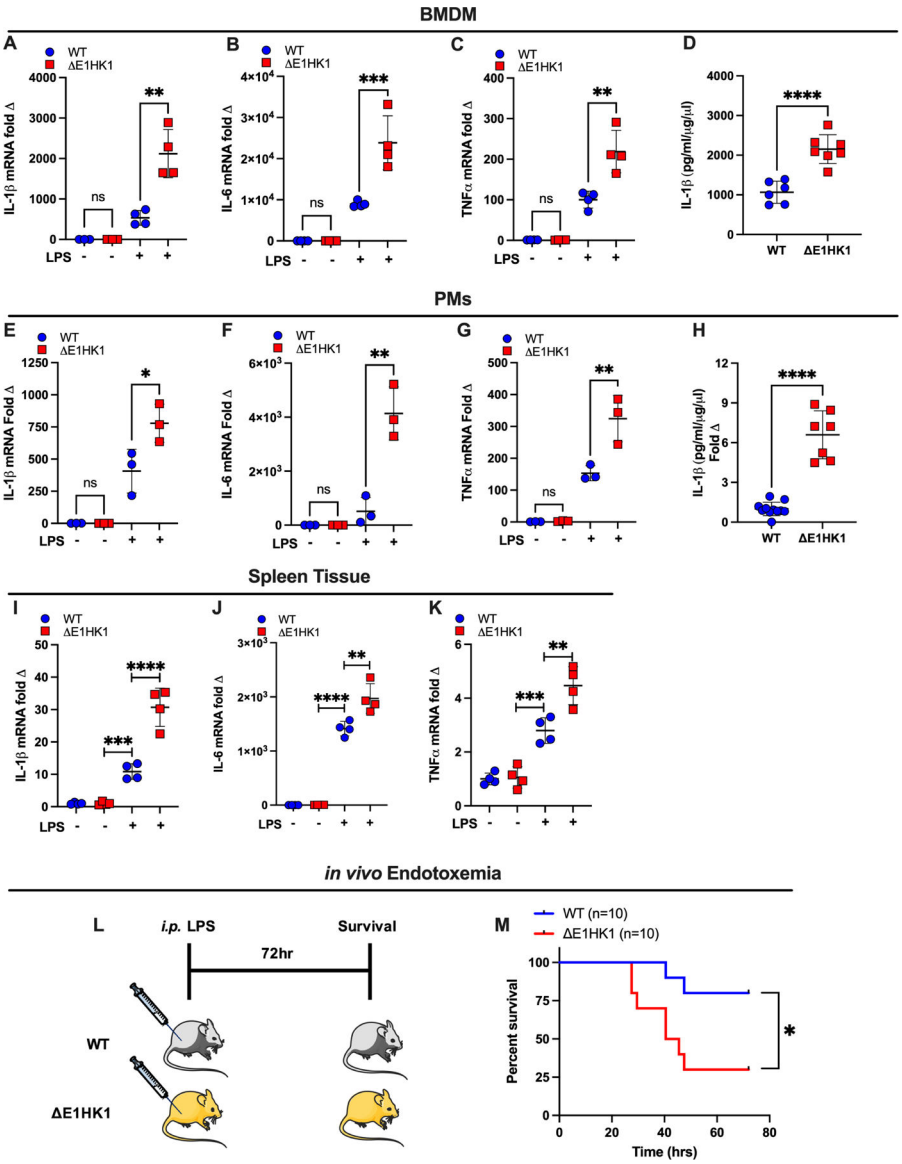

Figure 3. HK1 mitochondrial dissociation increases inflammatory cytokine production *in vitro & in vivo*

(A-C) Inflammatory cytokine mRNA expression of IL-1β (A), IL-6 (B), and TNFα (C) from isolated BMDMs ± 6hrs LPS (200ng/ml) (n=4 mice per condition, one-way ANOVA and Tukey's post-hoc test).

(D) IL-1β ELISA from BMDM media ± 6hrs of LPS (200ng/ml) followed by 30min ATP (2.5mM), normalized to total protein (n=6–7 mice per condition, unpaired t-test).

(E-G) mRNA expression of IL-1β (E), IL-6 (F), and TNFα (G) from isolated PMs ± 6hrs LPS (300ng/ml) (n=3 mice per condition, one-way ANOVA and Tukey's post-hoc test).

(H) IL-1β ELISA from PM media ± 6hrs of LPS (300ng/ml) followed by 30min of ATP (2.5mM), normalized to total protein (n=7–10 mice per condition, unpaired t-test).

(I-K) mRNA expression of IL-1β (I), IL-6 (J), and TNFα (K) from splenic tissue after i.p. injection of mice with LPS (15mg/kg) for 4hrs. (n=4 mice per condition, one-way ANOVA and Tukey's post-hoc test).

(L) Schematic of LPS-induced endotoxemia model. Mice were given i.p. injection of LPS (15mg/kg) and observed over 72hrs for survival.

(M) Survival curve of mice in LPS-induced endotoxemia model (n=10 mice per condition, survival curve log-rank Mantel-Cox test).

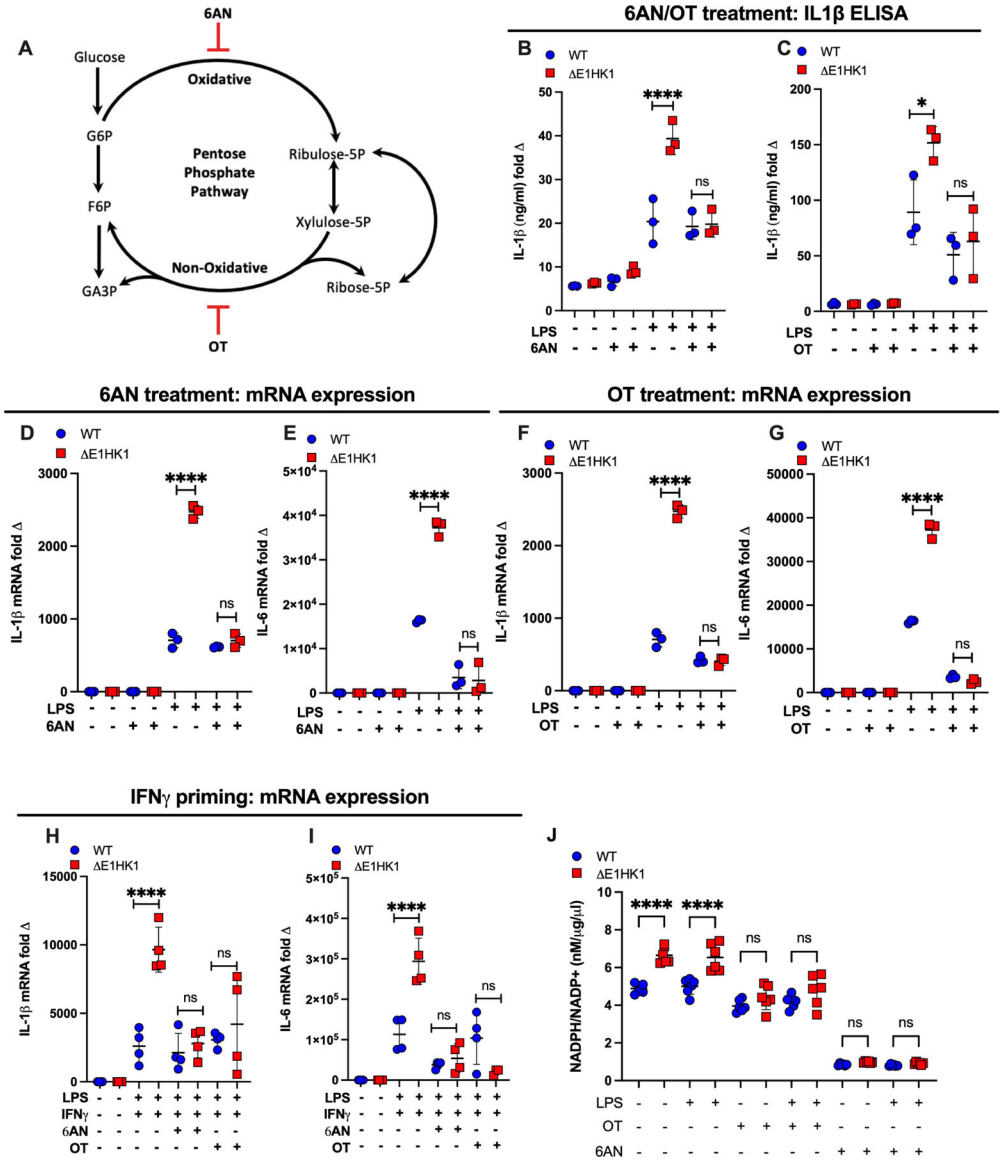

Figure 4. Inhibition of PPP reverses hyper-inflammation induced by HK1 mitochondrial dissociation

(A) Schematic of oxidative and non-oxidative branch of PPP with 6AN blocking the oxidative branch and OT blocking the non-oxidative branch.

(B-C) IL-1β ELISA from BMDM media after 4hrs of LPS (200ng/ml) ± 6AN (1mM) (B) or OT (50μM) (C) followed by 30min of ATP (2.5mM), normalized to total protein (n=3 mice per condition, two-way ANOVA and Tukey's post-hoc test).

(D-E) mRNA expression of IL-1β (D) and IL-6 (E) ± 4hr 6AN (1mM) or ± LPS (200ng/ml) (n=3 mice per condition, two-way ANOVA and Tukey's post-hoc test).

(F-G) mRNA expression of IL-1β (F) and IL-6 (G) ± 4hr OT (50μM) or ± LPS (200ng/ml) (n=3 mice per condition, two-way ANOVA and Tukey's post-hoc test).

(H-I) mRNA expression of IL-1β (H) and IL-6 (I) with ± 16hrs IFNϒ priming followed by ± 4hrs of LPS (200ng/ml) ± 6AN (1mM) and ± OT (50μM) (n=4 mice per condition, two-way ANOVA and Tukey's post-hoc test).

(J) NADPH/NADP+ ratio with ± 4hrs of LPS (200ng/ml) ± 6AN (1mM) and ± OT (50μM) (n=6 mice per condition, two-way ANOVA and Tukey's post-hoc test).

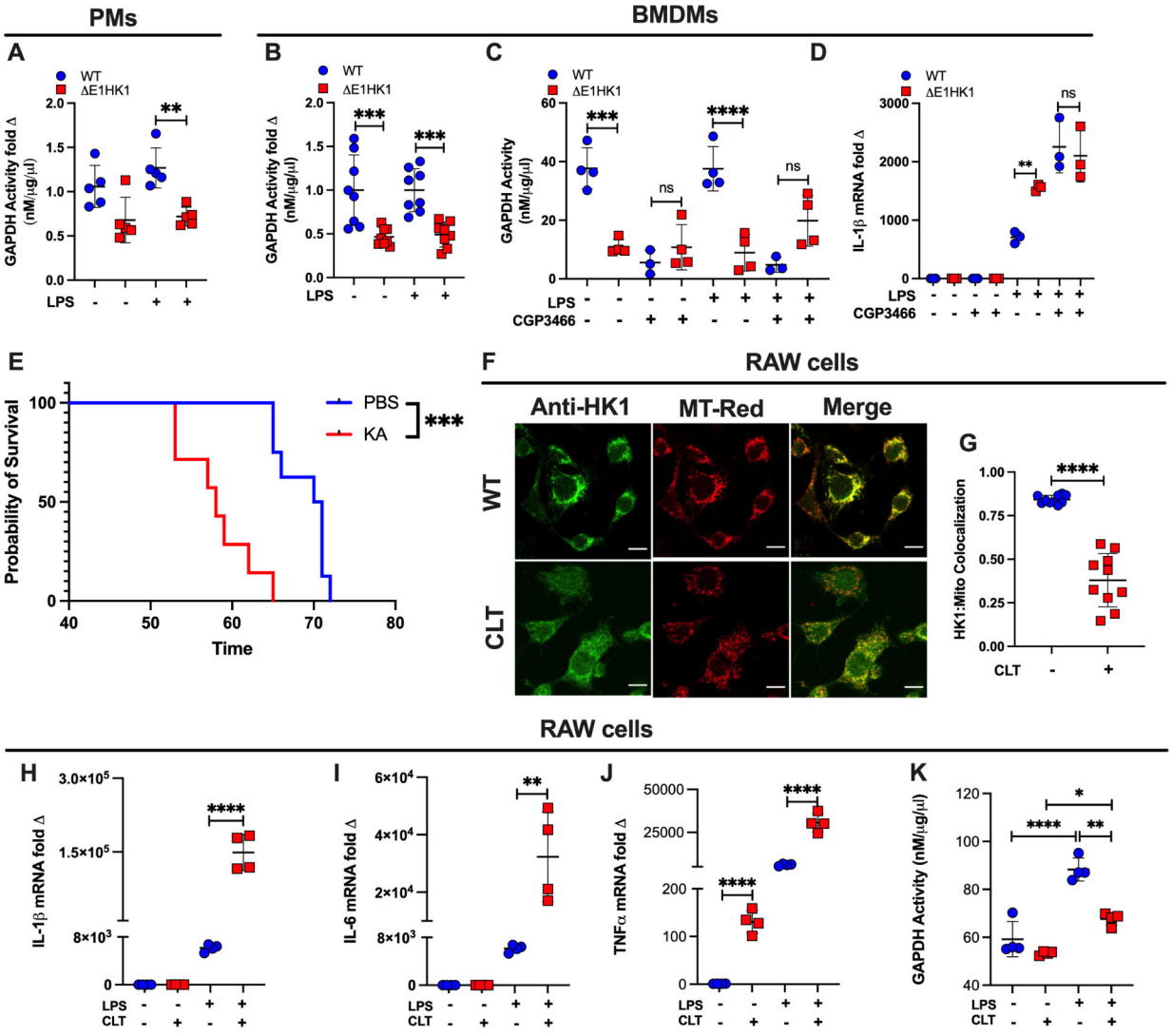

Figure 5. GAPDH activity is attenuated in macrophages with HK1 mitochondrial detachment

(A) GAPDH activity normalized to total protein in PMs treated with ± LPS (300ng/ml) (n=5 mice per condition, two-way ANOVA and Tukey's post-hoc test).

(B-C) GAPDH activity normalized to total protein in BMDMs ± LPS (200ng/ml) (B) and ± CGP3466 (GAPDH inhibitor) for 4hrs (C) (n=8 mice per condition for panel B and n=4 mice per condition for panel C, two-way ANOVA and Tukey's post-hoc test).

(D) IL-1β mRNA expression in BMDMs ± LPS and ± CGP3466 for 4hrs (n=3 mice per condition, two-way ANOVA and Tukey's post-hoc test).

(E) Survival curve of mice in LPS-induced endotoxemia model with or treatment with X [concentration] of KA (n=8 mice per condition, survival curve log-rank (Mantel-Cox) test).

(F-G) IF of HK1 and mitochondria (MT-Red) imaging in RAW264.7 cells ± clotrimazole (CLT) (20μM) (E) and mitochondrial to HK1 colocalization analysis (F) (n=10 cells per condition, unpaired t-test, scale bar = 15μm).

(H-J) mRNA expression of IL-1β (G), IL-6 (H), and TNFα (I) in RAW264.7 cells ± CLT (20μM) (n=4 replicates per condition, two-way ANOVA and Tukey's post-hoc test).

(K) GAPDH activity normalized to total protein in RAW264.7 cells ± CLT (20μM) (n=4 replicates per condition, two-way ANOVA and Tukey's post-hoc test).

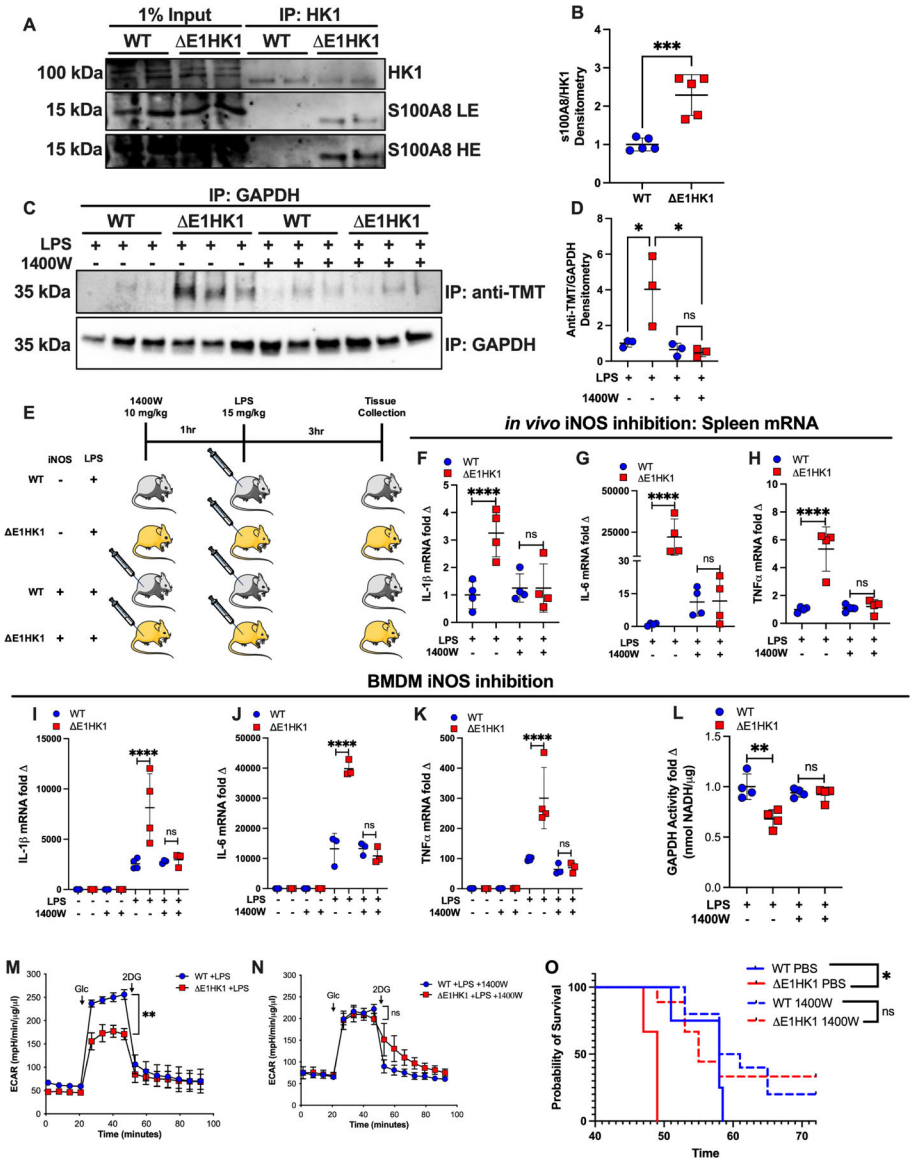

Figure 6. Cytosolic HK1 mediates GAPDH nitrosylation through S100A8/9 binding.

(A) Western blot of HK1 co-IP from BMDMs treated with LPS (200ng/ml) for 3hrs and probing for S100A8 binding. LE = Low-exposure and HE = high-exposure.

(B) HK1 co-IP western blot densitometry analysis of S100A8 divided by total HK1 eluted (n=5 mice per condition, unpaired t-test).

(C-D) Western blot of GAPDH IP and TMT switch nitrosylation assay of LPS (200ng/ml) treated BMDMs ± 1400W (10mg/kg) (C) and Western blot densitometry of anti-TMT normalized to total GAPDH eluted (D) (n=3 mice per condition, one-way ANOVA and Tukey's post-hoc test).

(E) Schematic of *in vivo* LPS (15mg/kg) ± 1400W (10mg/kg) i.p. injection experiment.

(F-H) Spleen tissue mRNA expression of IL-1β (F), IL-6 (G), and TNFα (H) from mice after i.p. injection of LPS ± 1400W (n=4 mice per condition, one-way ANOVA and Tukey's post-hoc test).

(I-K) mRNA expression of IL-1β (I), IL-6 (J), and TNFα (K) from isolated BMDMs ± 4hrs LPS (200ng/ml) ± 1400W (50μM) (n=4 mice per condition, one-way ANOVA and Tukey's post-hoc test).
(L) GAPDH activity normalized to total protein from BMDMs treated with LPS (200ng/ml) ± 1400W (50μM) (n=4 mice per condition, one-way ANOVA and Tukey's post-hoc test).
(M-N) ECAR trace of BMDMs treated for 5hrs of LPS (200ng/ml) (M) or 5hrs LPS ± 1400W (50μM) (N) (n=3–4 mice per condition, repeated measures two-way ANOVA and Tukey's post-hoc test, mean ± SEM).
(O) Survival curve of mice in LPS-induced endotoxemia model in the presence and absence of 1400W (n=10 mice per condition, survival curve log-rank (Mantel-Cox) test).

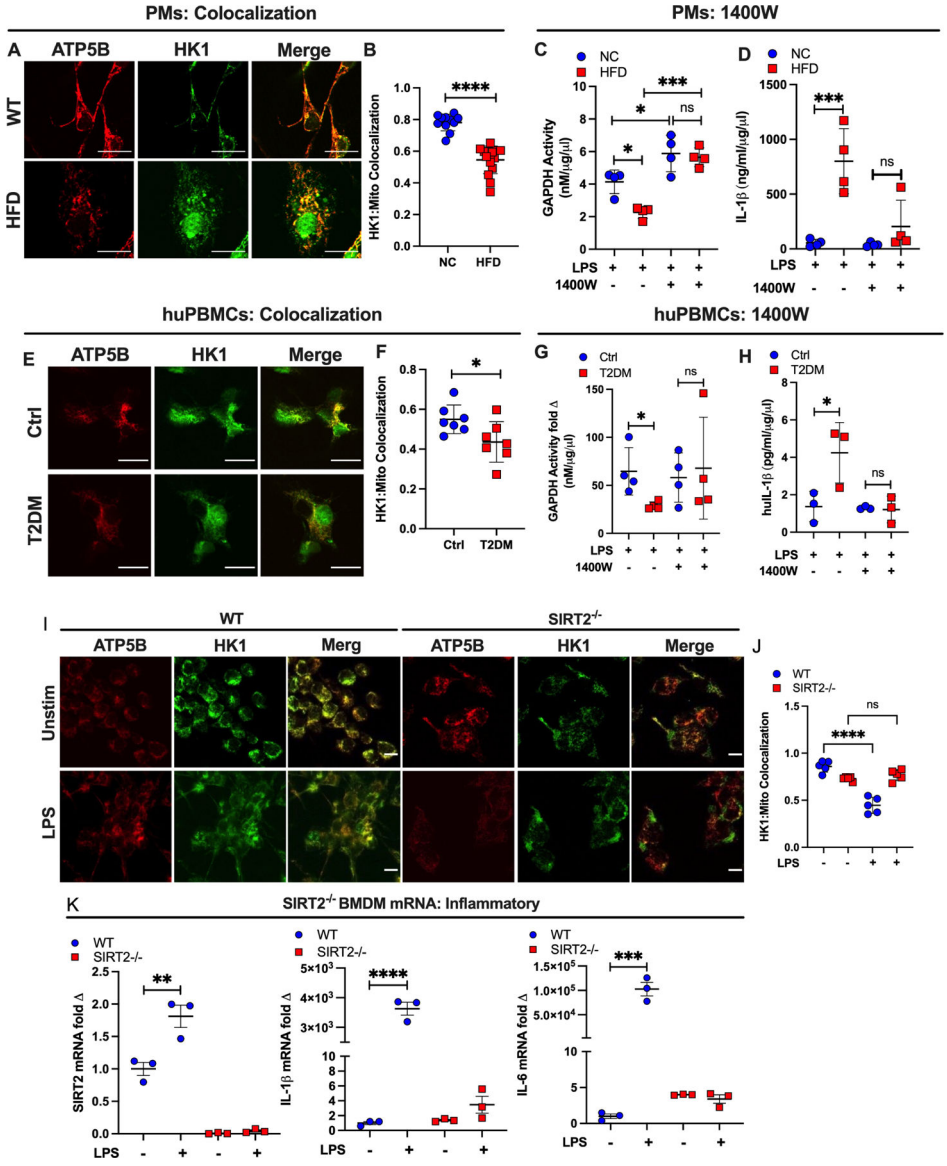

Figure 7. Diabetes is associated with HK1 mitochondrial dislocation and increased cytokine production

(A and **B)** Representative IF images probing for HK1 and mitochondria (using an antibody against ATP5B) in isolated PMs from NC and HFD mice (A) and colocalization analysis of IF images using Pearson's correlation coefficient (B) (n=11–15 cells per condition, unpaired t-test).

(C) GAPDH activity normalized to total protein in PMs isolated from NC and HFD treated with LPS (300ng/ml) ± 1400W (50μM) for 4hrs (n=4 mice per condition, two-way ANOVA and Tukey's post-hoc test).

(D) IL-1β ELISA from media of PMs treated with LPS (300ng/ml) for 6hrs and ATP (2.5mM) for 30min (n=4 mice per condition, one-way ANOVA and Tukey's post-hoc test).

(E-F) Representative IF images from normal control (Ctrl) and T2DM patients (E) and colocalization analysis of IF images (F) (n=7 images per condition, unpaired t-test).

(G) GAPDH activity normalized to total protein in huPBMCs treated with LPS (200ng/ml) ± 1400W (50μM) for 4hrs (n=4 patients per condition, two-way ANOVA and Tukey's post-hoc test).
(H) IL-1β ELISA from media of huPBMCs treated with LPS (200ng/ml) for 6hrs and ATP (2.5mM) for 30min (n=3 patients per condition, one-way ANOVA and Tukey's post-hoc test).
(I-J) Representative IF images from WT and *Sirt2*$^{-/-}$ BMDMs treated with LPS (I) and colocalization analysis of IF images (J) (n=5 images per condition, two-way ANOVA and Tukey's post-hoc test).
(K) *Sirt2*, IL-1β and IL-6 mRNA expression in BMDMs from WT and *Sirt2*$^{-/-}$ mice ± LPS for 4hrs (n=3 mice per condition, two-way ANOVA and Tukey's post-hoc test).

KEY RESOURCES TABLE

REAGENT or RESOURCE	SOURCE	IDENTIFIER
Antibodies		
S100A8 Rabbit Polyclonal Antibody	Proteintech	15792-1-AP; RRID:AB_10666315
ATP Synthase beta Monoclonal-Alexa Fluor 555	Thermo Fisher Scientific	MA1930A555; RRID:AB_2633316
GFP-tag Mouse Monoclonal Antibody	Proteintech	66002-1-Ig; RRID:AB_11182611
VDAC1/Porin Rabbit Polyclonal Antibody	Proteintech	55259-1-AP; RRID:AB_10837225
Hexokinase I (C35C4) Rabbit mAb	Cell Signaling Technologies	2024S; RRID:AB_2116996
Hexokinase II (C64G5) Rabbit mAb	Cell Signaling Technologies	2867; RRID:AB_2232946
IL-1β (3A6) Mouse mAb	Cell Signaling Technologies	12242; RRID:AB_2715503
GAPDH (14C10) Rabbit mAb	Cell Signaling Technologies	2118S; RRID:AB_561053
GFP-Trap Agarose	Chromotek	gta-20; RRID:AB_2631357
Binding Control Agarose Beads	Chromotek	bab-20; RRID:AB_2827547
Alpha-Tubulin Antibody	Proteintech	66031-1-Ig; RRID:AB_11042766
TMT Monoclonal Antibody (25D5)	Thermo Fisher Scientific	90075; RRID:AB_10854708
Beta-Actin Antibody	Proteintech	60008-1-Ig; RRID:AB_2289225
FLAG M2 mouse	Sigma-Aldrich	F1804; RRID:AB_262044
Goat anti-Rabbit IgG (H+L), Superclonal™ Secondary Antibody, Alexa Fluor 488	Thermo Fisher Scientific	A27034; RRID:AB_2536097
Donkey Anti-Mouse IgG (H+L) Antibody Horseradish Peroxidase (HRP)	Jackson ImmunoResearch	715-035-150; RRID:AB_2340770
Donkey Anti-Rabbit IgG (H+L) Antibody Horseradish Peroxidase (HRP)	Jackson ImmunoResearch	711-035-152; RRID:AB_10015282
Bacterial and virus strains		
EGFP (pHIV-Puro vector)	This paper	N/A
FLHK1-EGFP (pHIV-Puro vector)	This paper	N/A
TrHK1-EGFP (pHIV-Puro vector)	This paper	N/A
OMP-HK1-EGFP (pHIV-Puro vector)	This paper	N/A
FLHK1-K15R/K21R-EGFP (pHIV-Puro vector)	This paper	N/A
FLHK1-K15Q/K21Q-EGFP (pHIV-Puro vector)	This paper	N/A
Chemicals, peptides, and recombinant proteins		
Lactate Oxidase from Aerococcus Viridans	Sigma-Aldrich	L9795
β-Nicotinamide adenine dinucleotide phosphate sodium salt	Sigma-Aldrich	N8035-15VL
Pierce 16% formaldehyde	Thermo Fisher Scientific	28906
Clotrimazole	Sigma-Aldrich	C6019
2-Deoxy-D-glucose	Sigma-Aldrich	D8375
IFN gamma mouse recombinant protein	PeproTech	315-05-100ug
RNA stat 60	Tel Test Inc	CS-502
Novex™ 16% Tricine Protein Gels, 1.0 mm, 12-well	Thermo Fisher Scientific	EC66952BOX
Accutase	Sigma-Aldrich	A6964
Red Blood Cell (RBC) Lysis Buffer	Abcam	Ab204733

REAGENT or RESOURCE	SOURCE	IDENTIFIER
Macrophage-Colony Stimulating Factor (mCSF)-mouse	GenScript	Z02930
Methyl pyruvate	Sigma-Aldrich	371173
CGP 3466B maleate	Tocris	2966
Heptelidic Acid (Koningic Acid)	Cayman Chemical Company	14079
1400W dihydrochloride	Tocris	1415
6-Aminonicotinamide	Sigma-Aldrich	A68203
Oxythiamine chloride hydrochloride	Sigma-Aldrich	04000
DMEM with L-Glutamine	Corning	MT-10-017-CV
RPMI 1640 with L-Glutamine	Sigma-Aldrich	R1383
Digitonin	Sigma-Aldrich	D141
ProLong Gold Antifade Mountant with DAPI	Life Technologies	P36931
MitoTracker Deep Red FM	Thermo Fisher Scientific	M22426
Tetramethylrhodamine, Ethyl Ester, Perchlorate (TMRE)	Thermo Fisher Scientific	T669
Ultrapure O5:B55 LPS	Invivogen	tlrl-pb5lps
Crude O5:B55 LPS	Sigma	L2880
D-Glucose (U-13C6)	Cambridge Isotope Laboratories	CLM-1396-1
2-NBDG	Cayman Chemical Company	11046
Glucose-6-Phosphate Dehydrogenase (G6P-DH) from Leuconostoc mesenteroides	Sigma	10165875001
ATP	Sigma-Aldrich	A2383
Tween-20	DOT Scientific Inc	DSP20370-0.5
Cyclohexamide (HPLC)	Sigma-Aldrich	01810
TRUE Metrix Blood Glucose Test Strips 5	Trividia Health Inc.	N/A
Critical commercial assays		
NADP/NADPH-Glo kit	Promega	G9081
NAD/NADH-Glo kit	Promega	G9071
Duoset ELISA IL-1beta-mouse kit	R&D	DY401-05
Duoset ELISA TNFalpha-mouse kit	R&D	DY410-05
Duoset ELISA IL-6-mouse kit	R&D	DY406-05
Anti-HK1 Magnetic Beads IP kit	Sino Biological	MB101347-T38
Infusion HD kit	Clontech	638910
Glyceraldehyde 3 Phosphate Dehydrogenase Activity Assay kit	Abcam	ab204732
Thermo Scientific Pierce S-Nitrosylation Western Blot kit	Fisher Scientific	PI90105
Pierce BCA Protein Assay kit	Fisher Scientific	PI23225
Mitochondria Isolation Kit for Cultured Cells	Fisher Scientific	PI-89874
Deposited data		
Metabolomics Data		MassIVE: MSV000088899
Proteomics Data		MassIVE: MSV000088901
Mendeley Data		https://doi.org/10.17632/b2777d3sws.3

REAGENT or RESOURCE	SOURCE	IDENTIFIER
Experimental models: Cell lines		
Human: HEK293T	ATCC	Cat# CRL-3216
Human: HepG2	ATCC	Cat# HB-806
Mouse: RAW264.7	Prof. Jason Albert Wertheim (Northwestern University)	N/A
Mouse: primary bone marrow-derived macrophages	This paper	N/A
Mouse: primary peritoneal macrophages	This paper	N/A
Experimental models: Organisms/strains		
ΔE1HK1-C57BL/6J mice	This paper	N/A
WT C57BL/6J mice	This paper	N/A
SIRT2$^{-/-}$ -C57BL/6J mice	This paper	N/A
Oligonucleotides		
IL-1β mouse primers	IDT	Fwd: GTGGACGGGACGCTCTAC Rev: TTCACTGTTTGGTGCATGATT
TNFα1β mouse primers	IDT	Fwd: GCCTCTTCTCATTCCTGCTTG Rev: CTGATGAGAGGGAGGCCATT
IL-6 mouse primers	IDT	Fwd: CCTCTGGTCTTCTGGAGTACC Rev: ACTCCTTCTGTGACTCCAGC
MCP1 mouse primers	IDT	Fwd: AGCCAACTCTCACTGAAGCC Rev: GCGTTAACTGCATCTGGCTG
ARG2 mouse primers	IDT	Fwd: GGAAAGCCAATGAAGAGCTGG Rev: GCTTCCAACTGCCAGACTGT
PPARγ mouse primers	IDT	Fwd: GCTGGGGTATTGGGTCGC Rev: TTCCATCACGGAGAGGTCCA
CARKL mouse primers	IDT	Fwd: CACTTGGTCACATGGCAGGA Rev: CTTCAGAAACTCCGGGCTGT
HK1 mouse primers	IDT	Fwd: GTGGACGGGACGCTCTAC Rev: TTCACTGTTTGGTGCATGATT
HK2 mouse primers	IDT	Fwd: GAATGGGAAGTGGGGTGGAG Rev: TGTGGTCAAAGAGCTCGTCC
HK3 mouse primers	IDT	Fwd: CTGAGATGGAGGACACCGC Rev: CCACGCACACATATTGCACC

REAGENT or RESOURCE	SOURCE	IDENTIFIER
GCK mouse primers	IDT	Fwd: AGGGAACAACATCGTGGGAC Rev: TGGACTGGGAGCATTTGTGG
HKDC1 mouse primers	IDT	Fwd: AGATGGCTCAGAAAACGGGG Rev: GGGCCAGCTTCTTGTTCTCT
GPI mouse primers	IDT	Fwd: AAGGAGGTGATGCAGATGCT Rev: GCCCGATTCTCGGTGTAGT
PFK mouse primers	IDT	Fwd: TGGCAGACTATGTGTCTGGGGAGC Rev: GCTAGCACTGGGAGGGTGAGAGTC
ALDO mouse primers	IDT	Fwd: GCCGCAGCCAGTGAATCTCTCTTC Rev: TTCACAGACAACACCGCACACGAG
G6PD mouse primers	IDT	Fwd: TTTGTCCTATGCTGCTGCCACTGC Rev: GGCTGGAAGGGAGGTGATTCAGGT
PGD mouse primers	IDT	Fwd: CCGTCACCCTCATTGGAG Rev: GGACCACCTTAGGACCCTTC
RPE mouse primers	IDT	Fwd: TCTGTCATTCCTTCCTGCCCCTGG Rev: TCCAACCCAGTGGCACTTCCAAGA
RPIA mouse primers	IDT	Fwd: TCAATCTCATCAAGGGTGGA Rev: CATAACCAGCCACGATCTTCT
TKT mouse primers	IDT	Fwd: GGGCTGGTGTAACTCTGCAT Rev: CCCGGATGCTGATCTTATCT
TALDO mouse primers	IDT	Fwd: CCACAGAAGTTGATGCAAGG Rev: AGCTTCTTTGTAAAGCTCGATGA
GAPDH mouse primers	IDT	Fwd: TGGTGGACCTCATGGCCTACATGG Rev: TGAGGGAGATGCTCAGTGTTGGGG

REAGENT or RESOURCE	SOURCE	IDENTIFIER
TPI mouse primers	IDT	Fwd: TGAGCCGTTTCCACCGCCCTATTA Rev: GCTCCAACCATGAGTTTCCAGCCC
PGM mouse primers	IDT	Fwd: GTTCTCGGACCACATCGAGGGACA Rev: TGCAGGACAGGTTCCAGGGACAAA
PGK mouse primers	IDT	Fwd: AAGTCCTTCCTGGGGTGGATGCTC Rev: AGGGTTCCTGGTGCCACATCTCAG
ENO1 mouse primers	IDT	Fwd: TAGGCATCCACACCTGACCACCAG Rev: GGGCTCCAGACACTAGCTGGGAAG
PK mouse primers	IDT	Fwd: TTAGGCCAGCAACGCTTGTAGTGC Rev: AGATGCTGCCGCCCTTCTGTGATA
LDHA mouse primers	IDT	Fwd: CACTGACTCCTGAGGAAGAGGCCC Rev: AGCTCAGACGAGAAGGGTGTGGTC
PDHA1 mouse primers	IDT	Fwd: TGTGTGATGGTCAGGAAGCC Rev: CCGAGTGAAGGTGAAGCCAT
PDHB mouse primers	IDT	Fwd: AGTTGCCCAGTATGACGGTG Rev: CCAGCAAAGCCCATCTCTGA
DLD mouse primers	IDT	Fwd: TGGCAAAGACTTGGTGCAGA Rev: AAGCAGCTTCGACAGACACA
PC mouse primers	IDT	Fwd: GGGCGGAGCTAACATCTACC Rev: TATACTCCAGACGCCGGACA
MPC1 mouse primers	IDT	Fwd: CGGTAGATGCACTTCTGGGG Rev: GAAAGTCATCCGCCCACTGA
MPC2 mouse primers	IDT	Fwd: ACCTACCACCGACTCATGGA Rev: AGCACACACCAATCCCCATT

REAGENT or RESOURCE	SOURCE	IDENTIFIER
IDH mouse primers	IDT	Fwd: GGCACTGTCACACGTCACTA Rev: ATGGAAGCAATGGGGTTGGT
OGDH mouse	IDT	Fwd: CAGATGTCCTGCCTGACCTG Rev: TCGCAGCACATGGAAGAAGT
CS mouse primers	IDT	Fwd: CGGTTTGTCTACCCTTCCCC Rev: GGCAGGATGAGTTCTTGGCT
FH mouse primers	IDT	Fwd: GCAGCATCATGCCAGGAAAG Rev: ATTCCCCATGACTTGGGCTG
SDHC mouse primers	IDT	Fwd: ATAGCCTTGAGTGGAGGGGT Rev: CAGACCTGGGGTATTGCCAG
MDH mouse primers	IDT	Fwd: GACCTGTTCAACACCAACGC Rev: GGATGGTGGAGTTCACTGGG
18s mouse primers	IDT	Fwd: AGTCCCTGCCCTTTGTACACA Rev: CGATCCGAGGGCCTCACTA
ACTB mouse primers	IDT	Fwd: CCGTGAAAAGATGACCCAGAT Rev: GTACATGGCTGGGGTGTTG
S100A8 mouse siRNA	Dharmacon	20201
6PGD mouse siRNA	Sigma	001081274
iNOS mouse siRNA	Dharmacon	2886329G.1
Recombinant DNA		
FLHK1-pGFPN3	This lab	N/A
TrHK1-pGFPN3	This lab	N/A
GAPDH^{C247A} (pCMV3-C-FLAG vector)	This paper	N/A
Software and algorithms		
MetaboAnalyst 4.0	Chong et al., 2019	https://www.metaboanalyst.ca/
Scaffold	Proteome Software	http://www.proteomesoftware.com/products/scaffold/
Prism 8.0	GraphPad	https://www.graphpad.com/
PANTHER classification system	Gene ontology Unifying Biology	http://pantherdb.org/geneListAnalysis.do
Fiji/ImageJ	NIH	https://imagej.net/Fiji/Downloads RRID: SCR_002285
Other		
High Fat Diet (HFD; 60% kcal fat)	Research diets	Cat# D12492